Manuscript prepared for Atmos. Chem. Phys. Discuss.
with version 2.2 of the LaTeX class copernicus_discussions.cls.
Date: 6 April 2013

A compressed super-parameterization: test of NAM-SCA under single-column GCM configurations

J.-I. Yano[1], S. K. Cheedela[2], and G. L. Roff[3]

[1]GAME/CNRS, CNRS-INSU-Météo France, URA 1357, Toulouse, France
[2]Max Planck Institute for Meteorology, Hamburg, Germany
[3]CAWCR, GPO Box 1289K, Melbourne 3001, Victoria, Australia

Correspondence to: J.-I. Yano (jun-ichi.yano@zmaw.de)

Abstract

The NAM-SCA (nonhydrostatic anelastic model with segmentally-constant approximation) is a type of cloud-resolving model (CRM) with a highly-inhomogeneous distribution of finite volumes of varying sizes in a horizontal direction under a two-dimensional geometrical configuration. These finite-volume positions and sizes are dynamically adapted to achieve best performance with a limited number of finite volumes. The concept can be compared with "compression" techniques used for digital images. The physics are also limited only to a minimum microphysics in order to also enhance compression.

NAM–SCA is considered an intermediate between a CRM and a conventional parameterization. For this reason, it is called a *compressed super–parameterization* in the present study.

The present paper reports on a successful implementation of NAM-SCA as a subgrid–scale cloud–convection representation (parameterization) into single column versions of two global atmospheric models. ECHAM[1] and ACCESS[2] are chosen as the host models. A stand-alone single-column model (SCM) is also developed, in which the other physics are prescribed by observations. A simple radiation scheme is added as required.

Overall, the lowest-resolution ($\Delta x = 16\,\mathrm{km}$) NAM-SCA with the smallest domain size ($L = 32\,\mathrm{km}$) often works the best in terms of the errors for the precipitation rate, apparent heat source and moisture sink of the grid–box mean. Neither increase of resolution nor domain size leads to better performance in these respects until both cross the thresholds ($\Delta x \leq 1\,\mathrm{km}$ and $L \geq 256\,\mathrm{km}$). These results suggest that even a simple parameterization (with a small degree of freedom) can perform in a reliable way as long as it is constructed in a physically consistent manner. On the other hand, the prediction errors tend to be smaller for higher resolutions and larger domains. This tendency is clearer for the GATE[3] case than the TWP-ICE[4] case.

[1] ECMWF (European Centre for Medium Range Weather Forecasts) Hamburg version Atmospheric Model.

[2] Australian Community Climate and Earth-System Simulator.

[3] The Global Atmospheric Research Program's (GARP) Atlantic Tropical Experiment.

[4] Tropical Warm Pool-International Cloud Experiment.

1 Introduction

NAM-SCA (nonhydrostatic anelastic model with segmentally-constant approximation: Yano et al., 2010) is an intermediate between the traditional high resolution cloud-resolving models (CRMs), or large-eddy simulation (LES) models, and low–resolution parameterization schemes. From the CRM and LES point of view, NAM-SCA is a drastic "truncation" or "compression" under a finite-volume framework in combination with adaptive mesh-refinement capacity. Here, "compression" is used in the sense as used in data compression (cf. Yano et al., 2004). From a parameterization point of view, it constitutes a fully prognostic version of a mass-flux parameterization scheme. Recall that conventional mass-flux parameterization is constructed in a diagnostic manner, although recent schemes now tend to include certain prognostic features. NAM-SCA, which is developed under a direct "compression" of a CRM, can contain complete physics just as any CRMs can. Thus, it embodies a much more solid physical basis than any conventional parameterizations (cf. Yano et al., 2005). In this respect, NAM-SCA can be considered a prototype for future generic physical parameterizations.

A dry version of NAM-SCA was introduced by Yano et al. (2010) and a moist version with simplified microphysics was presented by Yano and Bouniol (2010) while the current version only includes warm microphysics. However, during the revision process for Yano and Bouniol (2010), we added a provision for modifying the fixed fall velocity of precipitating water from $v_T = 5\,\mathrm{ms}^{-1}$ to $v_T = 1\,\mathrm{ms}^{-1}$ for temperatures below the freezing point in order to mimic a snow process in a very crude manner. This modification has led to much more extensive stratiform clouds under a tropical mesoscale squall-line regime (Yano and Bouniol, 2011).

It is important to emphasize that NAM-SCA contains no other physics, no radiation nor boundary-layer processes. The present paper reports on the results obtained by implementing NAM-SCA as a subgrid–scale cloud–convection representation (parameterization) into single column (SCM) versions of general circulation models (GCMs), or GCM-SCM.[5] As a result of the implementation, NAM-SCA includes the available physics of a given GCM as grid-box

[5]This terminology is used throughout the paper in order to distinguish them from a stand-alone SCM introduced below.

scale processes.

The two GCM-SCMs adopted for this purpose are: ECHAM[6] and ACCESS[7], an Australian version of the UKMO Unified Model (UM). For the former, version 6 is used for the present study. For the latter, the 38 level ACCESS SCM used in the present study is based on a particular configuration of the UK Met Office's Unified Model, i.e. version 7.5 which was released by the UK Met Office in April 2010. This could be considered a first step for implementing NAM-SCA fully into GCMs under a three-dimensional configuration. A summary of default physics for the two GCMs are given in Appendix B and C. These two default physics are further compared in the Appendix D.

Additionally, a stand-alone single-column model (SCM) is developed. This version also couples NAM-SCA with large-scale processes, but with the other physics prescribed mostly by observations. Under this configuration, these prescribed physics do not interact with the NAM-SCA convective physics. Furthermore, a simple radiation scheme is added when necessary.

In the present study, NAM-SCA is placed within a GCM-SCM as a replacement of the default convection parameterization. Large-scale condensation as well as microphysics and cloud schemes are also turned off, because these processes are already handled by NAM-SCA. Importantly, NAM-SCA provides a cloud fraction in place of the cloud scheme by computing cloud distributions explicitly. Note that under this configuration, all the physical processes, except for microphysics, are evaluated only by using grid-box (domain-mean) values, neglecting all "subgrid-scale" contributions.

NAM-SCA can be, to some extent, understood as a variant of super-parameterization, as originally proposed by Grabowski and Smolarkiewicz (1999), and reviewed by Randall et al. (2003). However, a difference must also be emphasized. The idea of a super-parameterization is to place a CRM at a grid column in place of conventional physical parameterizations. In other words, all the physical descriptions are transferred into the super-parameterization. However in the present configuration, NAM-SCA only intends to replace convection and cloud parameteri-

[6]ECMWF (European Centre for Medium Range Weather Forecasts) Hamburg version Atmospheric Model.

[7]Australian Community Climate and Earth-System Simulator.

zations, and all the other physical descriptions within a GCM remain the same. *This also makes the computation burden of NAM-SCA much lighter than the super-parameterization.* Unfortunately, this comes with certain penalties which will be remarked upon when discussing the results. More importantly, NAM-SCA is "compressed" compared to a more convectional CRM, and this further reduces the computational cost.

For this reason, we propose to call this approach "compressed super-parameterization". Here, the concept of "compression" also includes those of physics: thus, only the minimum cloud microphysics is included under the present implementation. The spirit of minimum microphysics is developed by Yano and Bouniol (2010, 2011).

Two cases are considered in the present study: phase III from GATE (the Global Atmospheric Research Program's (GARP) Atlantic Tropical Experiment) and TWP-ICE (Tropical Warm Pool-International Cloud Experiment). Backgrounds of these two experiments are presented in Sect. 3. Qualitative differences of these two cases are also discussed. The numerical results are presented in Sect. 4. The paper is concluded with discussions on the results in Sect. 5. Table 1 lists the models used in the present study with corresponding sections indicated where given combinations are considered.

2 Formulation of the problem

The present section explains the formulation for implementing NAM–SCA into a GCM–SCM with only the pertinent points about the NAM–SCA formulation summarized. We refer to Yano et al. (2010); Yano and Bouniol (2010) for detailed formulation of the latter. The numerical resolution of NAM–SCA adopted in the present study is specified in Sect. 2.4.

2.1 Model formulation

As it stands for now, NAM-SCA is two dimensional and has the vertical velocity, w', potential temperature, θ, and the three water components (water vapor, $q_{\rm v}$, cloud water, $q_{\rm c}$, and precipitating water, $q_{\rm p}$) as prognostic variables. The zonal wind, u', is diagnosed from the vertical

velocity by mass continuity. Note that the prime is added to the two velocity components in order to indicate that only the deviation from the domain mean is considered. The domain mean zonal wind, $\bar{u}$, is prescribed by observations. The bar is also added to all the domain means below. Note that by assuming a periodic boundary condition, the domain-mean vertical velocity vanishes, though a domain averaged vertical velocity is implicitly applied as a part of large-scale forcing discussed below.

The formulation for NAM-SCA is given in Yano et al. (2010) for the dry case. The same formulation is retained in the present study with the minor modification that buoyancy is defined in terms of the virtual potential-temperature in place of the potential temperature. Similar equations are also adopted for the mixing ratios of water components. All the physical variables are horizontally advected by the total zonal wind, $u'+\bar{u}$, as described in Yano and Bouniol (2010).

The reference state potential temperature and water vapor are defined by an initial domain-averaged vertical profile for the stand-alone case. It is updated every host-model (SCM) time-step, ΔT, for the GCM-derived SCM (GCM-SCM) cases by a domain-averaged value. The latter procedure is justified by a multi-time scale asymptotic expansion assuming a slowness of large-scale processes compared to those of convective scales (cf. Ch. 11, Bender and Orszag, 1978; Sec. 3.20, Pedlosky, 1987).

Coupling between large-scale processes (those predicted by a host GCM-SCM) and convective-scale processes (those predicted within NAM-SCA) is achieved by writing a prognostic equation for any physical variable, φ, by

$$\frac{\partial \varphi}{\partial t} = -\left[\frac{\partial}{\partial x}(u'+\bar{u})\varphi + \frac{1}{\rho}\frac{\partial}{\partial z}\rho w'\varphi\right] + F_{\rm c} + \bar{F}_{\rm L} \tag{1}$$

Here, ρ is air density, $F_{\rm c}$ is a tendency of convective-scale physical processes evaluated directly inside NAM-SCA, and $\bar{F}_{\rm L}$ is a tendency of large-scale physical processes either prescribed or evaluated by other physical packages or by GCM-SCM.

The latter is defined by

$$\bar{F}_{\rm L} = -\left(\bar{\nabla}\cdot\bar{\boldsymbol{v}}\bar{\varphi} + \frac{1}{\rho}\frac{\partial}{\partial z}\rho\bar{w}\bar{\varphi}\right) + \bar{F}_{L,Physics} \tag{2}$$

where the first term is a tendency due to the large-scale advection and the second term is due to the physical processes. The latter is, in the stand-alone case, given by

$$\bar{F}_{L,Physics} = Q_R + \left(\frac{\partial \varphi}{\partial t}\right)_{flux} \tag{3}$$

with the radiative tendency (applies only to the potential temperature), Q_R, and a tendency due to the surface fluxes (applied both for potential temperature and moisture), which is defined by

$$\left(\frac{\partial \varphi}{\partial t}\right)_{flux} = \frac{\rho_0}{\rho}\frac{H_\mathrm{s}}{h_\mathrm{b}} \tag{4}$$

for the levels below the top, h_b, of the "boundary layer", $z \leq h_\mathrm{b}$. We otherwise set $(\partial\varphi/\partial t)_{flux} = 0$. Here, we assume a linear decrease of density weighted flux with height from the surface ($z = 0$) up to the top, $z = h_\mathrm{b}$, of the "boundary layer"; ρ_0 is the surface air density, H_s is the surface flux defined in such manner that H_s/w provides the dimension of φ, and we set $h_\mathrm{b} = 500\,\mathrm{m}$ in the present study.

In the GCM-SCM case, the large-scale tendency is simply estimated by

$$\bar{F}_\mathrm{L} = \frac{\bar{\varphi}^*(t+\Delta T) - \bar{\varphi}(t)}{\Delta T} \tag{5}$$

where $\bar{\varphi}^*(t+\Delta T)$ is the most updated state for a variable φ within the GCM-SCM before NAM-SCA is called.

Under this formulation, NAM-SCA is integrated in time from t to $t+\Delta T$. Note that both the large-scale zonal wind, $\bar{u}$, and the large-scale forcing, $\bar{F}_\mathrm{L}$, are fixed in time over this interval. In order to include all the processes within a given GCM to the large-scale tendency, $\bar{F}_\mathrm{L}$, NAM-SCA is called at the end of all the calls for evaluating tendencies. Unfortunately, the procedure in ACCESS turns out to be slightly complicated due to the fact that this model adjusts the boundary layer state based on all the given increments in a manner akin to implicit time-stepping (V. Barras, personal communication, 2011). NAM-SCA is called within ACCESS-SCM right before this boundary-layer adjustment step is applied, then the boundary-layer implicit time-stepping is called as a last procedure over a given time step.

The large-scale time step is taken as $\Delta T = 3\,\mathrm{h}$ for the stand-alone cases based on the data interval of testing cases, whereas we set $\Delta T = 12\,\mathrm{min}$ and $\Delta T = 20\,\mathrm{min}$, respectively, for ECHAM and ACCESS based on their default time steps.

As an important technical procedure, the last state, $\bar{\varphi}(t+\Delta T)$, of integration from NAM-SCA is directly copied to ACCESS as an update, rather than NAM-SCA indirectly providing a convective tendency. On the other hand, the large-scale tendency defined by

$$\frac{\bar{\varphi}(t+\Delta T)-\bar{\varphi}(t)}{\Delta T} \tag{6}$$

is provided to ECHAM. These procedures prevent a decoupling of the two models, NAM-SCA and the host model (GCM-SCM), which are running independently except for exchanges of some information. However, note that inputs from the host model to NAM-SCA are only in terms of the large-scale tendency as described above.

2.2 Cloud fraction and radiation

Along with the domain-averaged (grid-box mean) tendencies explained above, NAM-SCA also provides a cloud fraction to the host model. For this purpose, the cloud is defined as a point with the cloud mixing ratio larger than 10^{-5} ($10^{-2}\,\mathrm{g kg^{-1}}$). Under this definition, a mean cloud fraction over the period of ΔT is provided to the host model from NAM-SCA. This quantity is used in place of the one provided by an original cloud scheme for radiative transfer calculations within the host model. Note that this approach provides a definition of cloud fraction more consistent with the convective dynamics than any existing cloud schemes.

Recall that the present microphysics only includes liquid. Thus, in the ECHAM implementation, only the cloud liquid water mixing ratio is provided. On the other hand, in the ACCESS implementation, the cloud water is re-interpreted as a mixture of liquid and ice depending on the temperature by following a manner introduced by Grabowski (1998): above $-5\,^\circ\mathrm{C}$ the clouds all consist of liquid, below $-20\,^\circ\mathrm{C}$ all ice, and between $-5\,^\circ\mathrm{C}$ and $-20\,^\circ\mathrm{C}$ a mixture ratio based on a linear interpolation is assumed.

In principle, NAM-SCA can also provide an overlapping rate of clouds. However, for ease in the current implementation, the cloud overlapping rate is still defined within the radiation

code. Recall that a conventional cloud scheme does not provide cloud overlapping information. Radiation is called every 2 h in ECHAM, and every 3 h in ACCESS.

2.3 Diagnosis

For the purpose of the diagnosis, we introduce a term called the apparent source defined, in general, by

$$Q \equiv \frac{\partial \bar{\varphi}}{\partial t} + \left(\bar{\nabla} \cdot \bar{\boldsymbol{v}} \bar{\varphi} + \frac{1}{\rho} \frac{\partial}{\partial z} \rho \bar{w} \bar{\varphi} \right). \tag{7}$$

In the following, we designate the apparent source, as defined above, for the static energy, $C_p T + gz$, and the water vapor, q_v, by Q_1 and $-Q_2$, respectively. By following tradition (cf. Yanai et al., 1973), the minus sign is added to the water-vapor apparent source, and also both quantities are presented in units of K/day by multiplying $1/C_p$ and L/C_p on Q_1 and Q_2, respectively, where C_p is the heat capacity of the air at constant pressure, L is the latent heat and gz is the geopotential.

Errors of the simulations are measured by root-mean square (RMS) difference between the simulation and the observation. For the purpose of these diagnoses, we take the observational cycle, $\Delta T = 3\,\mathrm{h}$, also for calculating the tendencies from the model, as used for calculating the tendencies from the observation. Note that under this definition, noisiness of simulation for time scales less than ΔT does not contribute to this error measure when tendencies such as Q_1 and Q_2 are considered. Vertical average is performed in terms of the hydrostatic pressure, or alternatively in terms of weighted averaged with density in average over a geometrical coordinate.

Precipitation error is also calculated in terms of RMS difference. However, in this case, an instantaneous precipitation rate from a simulation is compared with an observed precipitation rate for the moment when the latter is available. By taking this definition, the noisiness of simulated precipitation directly affects the error measure. Due to this difference of the error estimate methods between Q_1 and Q_2 on the one hand, and the precipitation rate on the other hand, different aspects of the model errors are depicted in the following.

A key performance measure of NAM-SCA is the compression rate, which is a measure of numerical efficiency. It is defined as the ratio between the total number of mesh-segments and that with a full resolution. The lower values imply the model is better compressed.

2.4 Numerical setups for NAM-SCA

In testing NAM-SCA performance, both the minimum horizontal model resolution, Δx, and the horizontal domain size, L, for ranges of $\Delta x = 0.5$–$16\,\mathrm{km}$ and $L = 32$–$512\,\mathrm{km}$ are modified. Both parameters are increased by a factor of two over these ranges. In the following the simulation errors are summarized as functions of Δx (horizontal axis) and L (vertical axis). Note that the choice of the range for both Δx and L is rather extreme, and it is obvious that in the low–resolution small domain limit, no convective dynamics would be properly simulated. The key question to be asked here is how NAM–SCA works under these extreme limits as a subgrid–scale cloud–convection representation.

The compression threshold is kept to a standard value in the present study. We refer to Yano et al. (2010) for model behavior depending on the compression rate.

Stretched vertical coordinates are used with a lowest layer depth Δz_0, and gradually stretched as Δz_n up to the model top level, H. A rigid top boundary condition is assumed as in the case with Yano and Bouniol (2010). The full and the half levels are chosen identical to those given by the host model as an initial condition with ACCESS. The vertical coordinate also closely follows that of the host model with ECHAM.

In order to prevent the reflection of gravity waves from the rigid top, a sponge layer is added to the top layers of the model, in which all the physical variables are damped to the reference values with a damping rate, λ_{R}, which is linearly increased from the bottom, $z_{1,R}$, of the sponge layer to a height, $z_{2,R}$, above which the maximum value $\lambda_{\mathrm{R}} = 1/\tau_R$ defined in terms of the damping time-scale, τ_R, is used. All the model parameters are listed in the Appendix. The original NMA-SCA codes are available from ftp://cnrm-ftp.meteo.fr/pub-moana/yano/nam-sca/.

3 Study cases: GATE and TWP-ICE

Two observational cases are considered in the present study. A period from the GATE campaign and a full period of the TWP-ICE campaign. The observed precipitation time series for these two cases are shown in Fig. 1, which will be compared with results for subsequent simulations.

3.1 GATE

The Global Atmospheric Research Program's (GARP) Atlantic Tropical Experiment (GATE) was run during 1974 over the tropical Atlantic with the aim of establishing the thermodynamic budgets associated with tropical convection. The present study only considers the Phase III period: 00Z 30 August 1974 to 24Z 18 September 1974. This period has already been adopted for numerous studies by CRMs (e.g. Grabowski et al., 1996; Xu and Randall, 1996).

Observations are available over 19 vertical levels and every three hours with one degree resolution over a $9^\circ \times 9^\circ$ square within 4–14° N, 19–28° W. The data set is publicly available at http://kiwi.atmos.colostate.edu/scm/gate.html, which is originally provided from Michio Yanai's group at UCLA. Data were objectively analyzed by K. Ooyoma and J.-H. Chu from sounding data during the project (Esbensen et al., 1982; Sui and Yanai, 1986). Following Grabowski et al. (1996), data averaged over the $9^\circ \times 9^\circ$ array is used in the present study. The 3-h data sets from Thompson et al. (1979) and Cox and Griffith (1979) are used, respectively, for surface fluxes and radiative heating forcing in stand-alone calculations. The 6-hourly surface precipitation rate derived from radar observations (Hudlow and Patterson, 1979) is used for the validation of the simulations.

The observational domain is situated in the middle of a zone of easterly waves, which are often associated with squall-line convective systems. During the 20-day observation period, three squall-line convective systems (fast-moving mesoscale convective systems) were identified (days 6, 14, 18) which were typically followed by non-squall convective systems (slowly-propagating mesoscale convective systems) and then scattered convection. We refer the reader to Houze and Betts (1981) for an observational review.

3.2 TWP-ICE

The Tropical Warm Pool-International Cloud Experiment (TWP-ICE) took place over Northern Australia from 20 January to 13 February 2006 with an intensive observational period (IOP) from 22 January to 12 February (May et al., 2008). The observational network encompassed the Tiwi Islands and Darwin (main land) over an area with a radius of approximately $150\,\mathrm{km}$. The campaign was organized during the Australian monsoon period with the active period (13–25 January) followed by a suppressed to break period for the remaining of the campaign. The area is, in contrast to the GATE area, dominated by land forcing. With proximity to the main land, the Tiwi Islands experience strong land forcing. The strong forcing frequently leads to thunderstorm so regular and violent that they are locally called *Hectors*.

The large-scale forcing used here is based on a variational analysis method using sounding, radar, flux, and satellite observations during the campaign (Xie et al., 2010). Data is given in 3-h interval with a vertical resolution of $25\,\mathrm{hPa}$ from the surface ($1015\,\mathrm{hPa}$) to $40\,\mathrm{hPa}$ for the 25-day period. For stand-alone calculations the surface flux is taken from ECMWF analysis for large-scale forcing. Radiation is calculated every 3 h by taking a radiation code from the NCAR Community Climate Model 2 (CCM2: Kiehl et al., 1994). Precipitation rate is also available every 3 h in the TWP-ICE case. Studies have already been performed using this large-scale forcing set by Varble et al. (2011). Convection during TWP-ICE is also studied by Wapler et al. (2010) by taking a nesting approach.

3.3 Characterizations: free ride

As a particular characteristic of tropical atmospheric variability, the relationship

$$w\frac{\partial\bar{\varphi}}{\partial z}\simeq Q \tag{8}$$

is approximately satisfied for potential temperature (static energy) and, to a lesser extent, water vapor (cf. Fig. 1, Yano, 2001). This relation is known as “free ride” (Fraedrich and McBride, 1989) for the potential temperature, and it arises from the weak horizontal temperature gradients

(WTG: Sobel et al., 2001) over the tropics. The "free ride" may furthermore be re-interpreted in a slightly more general manner as

$$\bar{F}_{\rm L} \simeq Q. \tag{9}$$

A major qualitative difference of the present two study cases is also well elucidated by examining the generalized "free ride" balance (Eq. 9). In order to see it, scatter plots between large-scale forcing, $\bar{F}_{\rm L}$, and apparent source, Q, are plotted for the static energy (heat budget) and water vapor (moisture budget) for both study cases in Figs. 2 and 3, respectively.

The most striking difference between the two study cases is the magnitude of the large-scale forcing; it is ten times stronger for the TWP-ICE case than the GATE case. Difference by an order of magnitude in forcing also leads to drastically different model performances for these two cases: forcing is so strong for the TWP-ICE case that the whole column more or less destabilizes as a whole, making it difficult *not to* induce convective precipitation.

It may also be worthwhile to more closely examine the degree that both cases satisfy "free ride". In the GATE case, free ride is well satisfied both for heat and moisture budgets, though the slopes are about 10 % gentler than expected. On the other hand, in the TWP-ICE case, the moisture budget is noticeably away from "free-ride"with the slope -0.77. The gentler slope implies that convection consumes moisture at a substantially slower rate than the large-scale supplies. Note however that a rather gentle slope is mostly defined by weak forcing regimes. It is seen that in a strong forcing regime, the slope becomes much closer to -1. On the other hand, the heat budget satisfies the "free ride" better than the GATE case with the slope much closer to -1 (-0.96).

3.4 Characterizations: moist-static energy profile

In order to further delineate differences between the two study cases, we recall a basic reason for a convection parameterization to be required for global models. As pointed out by Riehl and Malkus (1958) (see also Yano, 2009), it is needed to close the heat budget as defined by the moist-static energy over the tropics. Here, the moist-static energy is defined by

$$h = C_p T + L q_{\rm v} + g z \tag{10}$$

in terms of: specific heat at constant pressure, C_p; temperature, T; latent heat of condensation, L; water-vapor mixing ratio, $q_{\rm v}$; acceleration of gravity, g; and geometric height, z. Over the ascending branch of the Hadley–Walker circulation, the moist-static energy represents a temporal tendency to increase and decrease at the surface and the tropopause levels, respectively, due to both horizontal advections and diabatic heating (surface flux and radiative cooling). Recalling that the moist-static energy is an approximately conserved quantity under moist-convective processes, the only way to close this budget is by its upwards transport, as expected. However, the large-scale average moist-static energy typically has a minimum at middle troposphere heights. This leads to upgradient transport in the upper troposphere when this vertical transport is due to the large-scale "resolved" motion. Riehl and Malkus (1958) proposed that the only way to resolve this dilemma was to assume an isolated transport process, "hot towers", that can advect the surface-level moist-static energy to the tropopause level without *substantial*[8] mixing. Since these "hot towers" are very localized, they are not well resolved by conventional GCMs, thus they must be represented in a parametric manner. This is one main reason why a convective parameterization scheme is required for GCMs.

Conversely, the strength of the mid-level moist-static energy minimum can be considered as a measure of the degree to which a convective parameterization scheme is required for a given situation. Interestingly, Aspliden (1976) shows that the moist-static energy minimum tends to be weaker during convectively more active periods (see his Fig. 1a). In order to see this same point, we plot time-height sections of the moist-static energy for the two study cases in Fig. 4.

The GATE case (Fig. 4a) is a typical repesentation of the tropical situation expected from Rhiel and Malkus' "hot-tower" hypothesis where the moist-static energy minimum is well maintained throughout the period. In this case, a convective parameterization is clearly required in order to properly describe the heat budget by a GCM. On the other hand, with the TWP-ICE case (Fig. 4b), we see that the moist-static energy is relatively well mixed vertically during the first 8 days, corresponding to an active monsoon period. On day 5, when the strongest rain-

[8]Note that the strict application of a non-entraining plume hypothesis, which they proposed at a very technical level, should not be confused with a more fundamental conceptual insight that they have brought to the tropical heat budget debate.

fall event occurred during the campaign, we see that the moist-static energy minimum almost disappears. Under this situation, moist convection could be handled *almost* without convective parameterization, especially when a modestly high horizontal-resolution (say $30\,\mathrm{km}$) could be adopted. This marks the second major characteristic difference between these two cases.

4 Results

4.1 Results with default GCM-SCMs

In order to establish a reference point for assessing the impacts of implementing NAM-SCA, the results of the two GCM-SCMs under default physics are first presented. Figures 5 and 6 show the precipitation time series simulated by default physics of ECHAM and ACCESS, respectively, for the GATE (a) and the TWP-ICE (b) cases. Note that for both ECHAM and ACCESS cases, the instantaneous precipitation time series are shown. These tend to be very noisy, reflecting the problem associated with quasi–equilibrium (statistical equilibrium) hypotheses adopted for convection in both models as demonstrated by a more idealized setting by Yano et al. (1998): refer especially to their discussions associated with Figs. 2 and 6.

RMS errors for these simulations are $1.08\,\mathrm{mmh}^{-1}$ and $0.868\,\mathrm{mmh}^{-1}$, respectively for the GATE and the TWP-ICE cases with ECHAM, and $2.27\,\mathrm{mmh}^{-1}$ and $1.30\,\mathrm{mmh}^{-1}$, respectively for the GATE and the TWP-ICE cases with ACCESS. The errors are 2.1 and 1.5 times larger for ACCESS compared to ECHAM, respectively, for the GATE and the TWP-ICE cases. The spikiness of the ACCESS-simulated precipitation clearly contributes to these higher errors. Even with ECHAM, the increased difficulties found in simulating the GATE precipitation time series rather than the TWP-ICE case due to its weaker large-scale forcing is clearly seen.

The time-height sections of Q_1 and Q_2 simulated by ECHAM-SCM and ACCESS-SCM default physics are shown in Fig. 7 and 8, respectively, for the GATE case. The same results for the TWP-ICE case are shown in Fig. 9 and 10, respectively. GATE RMS errors are $2.0\,\mathrm{Kday}^{-1}$ for both Q_1 and Q_2 for ECHAM-SCM, whereas they are $2.65\,\mathrm{Kday}^{-1}$ and $2.70\,\mathrm{Kday}^{-1}$, respectively, for ACCESS-SCM. ECHAM errors are about 25 % less than those by ACCESS both

for Q_1 and Q_2. Reflecting the spikiness of precipitation time series for ACCESS-SCM, the height-time sections of Q_1 and Q_2 are also spikier for the ACCESS-SCM than ECHAM-SCM. Clearly spikiness of the former contributing to larger errors.

TWP-ICE RMS errors with Q_1 and Q_2 are $2.62\,\mathrm{K\,day^{-1}}$ and $5.15\,\mathrm{K\,day^{-1}}$, respectively, for ECHAM-SCM, and $3.83\,\mathrm{K\,day^{-1}}$ and $5.09\,\mathrm{K\,day^{-1}}$, respectively, for ACCESS-SCM. A larger error with Q_2 for ECHAM-SCM than ACCESS-SCM is rather surprising considering all the major drying events in the first five days are better simulated by ECHAM-SCM compared to ACCESS-SCM. However, we note that in ECHAM-SCM, the Q_2 errors are more homogeneously distributed, which accumulates into a larger error in integral.

In the following, the RMS errors have been normalized by the corresponding default GCM-SCM results. When the stand-alone cases are presented, the errors are normalized by taking the ACCESS cases. Note that in order for a stand-alone case to beat the corresponding default ECHAM case, the normalized precipitation error must be less than 0.48 and 0.67, respectively, for the GATE and TWP-ICE cases.

4.2 Stand-alone case: GATE

4.2.1 Overview

A summary for the stand-alone GATE case is given in Fig. 11. The first point to make is a tendency for the compression rate to uniformally decrease diagonally from the lower right to the upper left, in a direction of an increasing maximum segment number, N_x. With only two segments (lower right), the compression is unity while at the highest resolution limit (upper left), the compression rate is enhanced almost to 0.1. The enhancement of compression is roughly logarithmic: as the resolution is increased by twice, compression improves by a constant rate. This tendency is common for all the following cases.

As for the error distributions, probably the most striking aspect here is that the best performance is obtained for Q_1, and Q_2 when only with the two volume elements (segments) are placed in a 32-km domain. Though the best precipitation result is attributed to the highest-resolution case ($\Delta x = 0.5\,\mathrm{km}$ and $L = 512\,\mathrm{km}$), the second best still falls again to the same

lowest-resolution case. Recall that the scale for the GATE observational network is about 900 km (cf. Sect. 3.1).

Error distributions for both Q_1 and Q_2 are quite similar: the best result is always obtained with domain size $L = 32\,\mathrm{km}$ when the resolution is fixed equal to or above $\Delta x = 1\,\mathrm{km}$. As soon as the domain size is doubled, the performance suddenly worsens. This tendency is the most obvious when $\Delta x = 16\,\mathrm{km}$ and is least dramatic when $\Delta x = 2\,\mathrm{km}$ for Q_1. In order to overcome this general tendency, a relatively high horizontal resolution, $\Delta x = 0.5\,\mathrm{km}$, must be taken. In this latter case, errors tend to decrease gradually as domain size increases.

An overall similar tendency is also found with the precipitation error distribution: the lowest-resolution case provides the second best result. As soon as either the resolution or the domain size is doubled, the model performance suddenly worsens. However, in contrast to the case with Q_1 and Q_2, the model performance gradually improves both with increasing resolutions and domain sizes beyond this point.

Note that the precipitation prediction often performs better than the default ECHAM case (0.48). However, the prediction of Q_1 and Q_2 never dramatically over-performs even against the ACCESS case.

4.2.2 The case with $\Delta x = 16\,\mathrm{km}$ and $L = 32\,\mathrm{km}$

In the case with $\Delta x = 16\,\mathrm{km}$ and $L = 32\,\mathrm{km}$, convective towers never develop due to the low-resolution and the high truncation, as expected, and all the precipitation happens as a result of relatively gentle ascent leading to a drizzling over one of the 16-km wide segments. By design, the model forms a simple symmetric Bernard-convection like cell with the magnitude of the vertical velocity never exceeding $1\,\mathrm{ms}^{-1}$, and both cloud and precipitation-water mixing-ratio remains well below $1\,\mathrm{gkg}^{-1}$ throughout the simulation. The circulation direction is somehow fixed with the right-side finite-volume segment always ascending and the left-side finite-volume segment always descending except for short periods of oscillatory behavior.

The precipitation time series obtained by this simulation is shown in Fig. 12a. Time-height sections for Q_1 and Q_2 for observed, modelled and the differences are shown in Fig. 13. The overall matching of Q_1's evolution is rather impressive except for the slightly spiky behavior.

The spikiness is presumably due to a need for a finite amplitude trigger in order to induce these "large-scale" precipitating "convection", as well as a difficulty of sustaining it continuously without smaller-scale contributions. On the other hand, defects of the simulation are more evident for Q_2: the surface tends to always be over moistened. A further anomalous moistening tendency is seen in the free troposphere (vertical levels 2–8 km), occasionally, for example for days 8–10. It is associated with a gradual re-evaporation of an existing cloud in an ascending column during a period with relatively weak large-scale forcing.

Moistening of the boundary layer leads to an enhanced conditional instability, making the system easier to sustain moist convection without smaller-scale circulations. Needless to say this tendency leads to substantial prediction error in the moisture field (cf. Sect. 4.5). It suggests an importance of a coupling between the boundary-layer processes and convection, which is not considered herein.

Note that the purpose of the exercise here is not at all for simulating the convective dynamics. The key point is completely other way round: in spite of the fact that the convective dynamics are not at all properly represented under this extreme low–resolution and small domain size, the grid–box mean outputs examined are not only reasonable, but even better than the cases in which the convective dynamics are much better represented.

4.2.3 Other cases

Figure 12b and c provide two more examples of the precipitation time series from the stand-alone GATE simulations. The highest resolution case ($\Delta x = 0.5\,\mathrm{km}$ and $L = 512\,\mathrm{km}$: b) has smaller RMS error than the case with $\Delta x = 16\,\mathrm{km}$ and $L = 32\,\mathrm{km}$, however, it always remains noisy, and arguably, certain periods (e.g. 0–4 days) are better simulated by $\Delta x = 16\,\mathrm{km}$ and $L = 32\,\mathrm{km}$. The third case with $\Delta x = 4\,\mathrm{km}$ and $L = 256\,\mathrm{km}$ (c) presents a tendency for the deterioration of precipitation as we move away from the best cases: the precipitation time series becomes spikier as we move away from these two best simulations.

Three more examples of time-height sections for Q_1 and Q_2 are shown in Fig. 14. All cases are overall comparable with the best case shown in Fig. 13, although the evolution tends to be slightly noisier in these cases. Note especially that an anomalous cooling tendency is noticed in

the middle-row case ($\Delta x = 1\,\mathrm{km}$ and $L = 256\,\mathrm{km}$) in Fig. 14a. On the other hand, an anomalous moistening tendency found in the lowest-resolution case (Fig. 13b) is much reduced in these three cases (Fig. 14b).

Finally, time-longitude sections for precipitation are shown in Fig. 15 for four high-resolution, large-domain cases: (a) $\Delta x = 0.5\,\mathrm{km}$ and $L = 512\,\mathrm{km}$; (b) $\Delta x = 1\,\mathrm{km}$ and $L = 512\,\mathrm{km}$; (c) $\Delta x = 2\,\mathrm{km}$ and $L = 256\,\mathrm{km}$; (d) $\Delta x = 4\,\mathrm{km}$ and $L = 256\,\mathrm{km}$. All these cases simulate the three major squall-line events as well as subsequent development of a non-squall line system and scattered convection after each squall-line event well. The far-left frame (a) is the highest resolution case with resolution and domain size decreasing to the right. Note that even with a relatively low-resolution ($\Delta x = 4\,\mathrm{km}$) with a modest domain size ($L = 256\,\mathrm{km}$: d), all these convective coherencies are still well simulated. This again demonstrates the capacity of NAM–SCA for successfully simulating convective organization, as already demonstrated by Yano and Bouniol (2010). It may also be important to emphasize a stability of the solution against change of the horizontal resolution, demonstrating a robustness of the numerical algorithm adopted for NAM–SCA.

Here, it is important to re-iterate the main point: in spite of the fact that all these runs simulate the mesoscale convective organization well, their overall performance on thermodynamic tendencies as measured by Q_1 and Q_2 never exceed that of the case with just two segments, in which no realistic convective sub-domain feature is simulated. It further suggests that inclusion of realistic convective elements, such as mesoscale organization, is not necessarily a crucial ingredient for improving convective parameterization. The success of the two-segment case rather suggests that a very crude scheme may work better than a more complex one as long as it provides a consistent description of convection processes.

4.3 Stand-alone case: TWP-ICE

4.3.1 Overview

Error distributions for the TWP-ICE case are summarized in Fig. 16. Basically, the tendency of error distributions is similar to the stand-alone GATE case: an increase of both resolution

and domain size does not necessarily lead to improved model performance. Overall, both resolution and domain size must be increased beyond thresholds in order to obtain a better result than a lower-resolution, smaller-domain case. However, the details are very different, and the distributions are more irregular than in the GATE case, especially for precipitation.

Most notably, the best precipitation prediction is obtained for the lowest resolution case. However, the error minimum moves to the case with $\Delta x = 2\,\mathrm{km}$, $L = 32\,\mathrm{km}$ and $\Delta x = 0.5\,\mathrm{km}$, $L = 64\,\mathrm{km}$ for Q_1 and Q_2, respectively. It is intriguing to note that the latter case ($\Delta x = 0.5\,\mathrm{km}$ and $L = 64\,\mathrm{km}$) performs the worst both for precipitation and Q_1.

Note that the overall performance with respect to Q_1 and Q_2 predictions is not at all impressive in the TWP-ICE case: the Q_2 error is never less than the default ACCESS case. Though the Q_1 error is occasionally less than the default ACCESS case, it never performs more than 3 % better. On the other hand, the performance of precipitation prediction is much better with NAM-SCA than both default ACCESS and ECHAM (with a normalized error 0.67) cases. The out-performance of the default GCM-SCMs by the TWP-ICE case presumably reflects the lack of a strong need for convective parameterization, as already discussed in Sect. 3.

Another problem here may be a lack of ice microphysics in NAM–SCA. Varble et al. (2011) emphasize an important role played by ice in cloud microphysics during TWP–ICE.

4.3.2 Examples

Some examples of the domain-mean precipitation are shown in Fig. 17. All the simulations predict all the major precipitation events correctly. The degree of accuracy of predictions rather depends on the noisiness of the time series. The two-segment case (a) is not necessarily the best in all aspects: the maximum precipitation rate for each event tends to be more over-predicted than the highest-resolution largest-domain case (b).

Examples of time-longitude sections of precipitation are shown in Fig. 18. As the case (Fig. 18a) with the highest resolution ($\Delta x = 0.5\,\mathrm{km}$) and the largest domain ($L = 512\,\mathrm{km}$) shows, the major convective event on day 5 is realized as a upwind-propagating squall-line system. Note that the system is dominated by deep westerlies for the first two weeks (cf. Fig. 5a in Xie et al., 2010), typical of an active period of the Australian monsoon. The first few rain-

fall events preceding this major event are simulated as less-organized downwind-propagating features. Less pronounced later precipitation events are realized as stationary systems. Remarkably these features are reproduced as both resolutions and the domain sizes decrease, as shown in Fig. 18b-d, though some inevitable deterioration is found. Note, however, that these simulated propagating features are, to some extent, artifacts of the modelling configuration. The actual observation domain is rather small (radius of 150 km), and observations suggest that these precipitation systems are part of much larger synoptic-scale processes (cf. Varble et al., 2011).

Figure 19 shows examples of time-height sections of (a) Q_1 and (b) Q_2, for the best (middle) and one of the worst (bottom) simulations in comparison with the observation (top). Note that the worst cases are not particularly bad, but a few exceptional erroneously spiky events deteriorate the overall performance. The case with $\Delta x = 0.5\,\mathrm{km}$, $L = 64\,\mathrm{km}$ is worth extra attention: this case gives the worst simulation in terms of both precipitation (Fig. 17c) and apparent heat source (Fig. 19a, bottom), however it gives the best simulation in terms of apparent moisture sink (Fig. 19b). It may also be worthwhile to emphasize that the mesoscale organization is relatively well reproduced (Fig. 18c) in spite of a small domain size.

It should be emphasized that even in this worst case run, the precipitation time series is in general correct with more or less all the rainfall events being correctly predicted (Fig. 18c), probably thanks to strong large-scale forcing acting during the TWP-ICE period. However, the time series is extremely spiky, and the maximum rainfall for each event over the period of day 10–13 is greatly overestimated. The apparent heat source, Q_1, is also well simulated in this case, but with a major exception of an overshoot of gravity waves found towards the end of the day 9 (Fig. 19a, bottom). This singular error clearly makes this simulation with the largest error for Q_1. Fortunately, this gravity-wave overshoot does not affect the moisture budget due to its mostly dry nature. It somehow allows the best simulation of the apparent moisture sink, Q_2, despite of the associated defects (Fig. 19b, middle).

Time-height sections for the best simulated case for Q_1 ($\Delta x = 2\,\mathrm{km}$, $L = 32\,\mathrm{km}$) and the worst simulated case for Q_2 ($\Delta x = 16\,\mathrm{km}$, $L = 256\,\mathrm{km}$) are shown in Fig. 19a, middle and Fig. 19b, bottom, respectively. The reasons for being the best and the worst are interpreted in

analogous manner as already developed for the case with $\Delta x = 0.5\,\mathrm{km}$ and $L = 64\,\mathrm{km}$. The few spiky moistening events during days 9–20 found in the worst Q_2 simulation are attributed to a relatively rapid disappearance of foggy clouds at a given level. The process is accomplished in association with local descent and adiabatic warming, leaving little trace in the apparent heat budget.

4.4 Results with NAM-SCA GCM-SCMs

4.4.1 Overview

Error summaries for the results with implementation of NAM-SCA into GCM-SCMs are shown in Fig. 20, 23, 25, 26. In spite of various difference in details, overall, the same conclusions as the stand-alone cases are drawn also by implementing NAM-SCA into GCM-SCMs: (i) one of the best performances is always obtained by the two-segment case (the lowest resolution); (ii) increase of both resolution and domain size does not necessarily lead to a reduction of model errors, but often the other way round; (iii) in order to gain an advantage using a high resolution and a large domain size, both should exceed threshold values.

Comparing those four cases (the GATE and the TWP-ICE cases both for ECHAM and ACCESS), more similarities are found in the same study case than in the same model. For this reason, in the following two subsections, the GATE and TWP-ICE cases are, respectively, discussed for both models.

4.4.2 GATE case

The GATE case (Figs. 20, 23) shows some benefits of implementing NAM-SCA into GCM-SCMs so that full physics are accessible for NAM-SCA: an overall model performance improves in respect to both stand-alone NAM-SCA and default GCM-SCMs. Probably the most remarkable is an improvement of the precipitation prediction for GCM-SCMs (b). The Q_1 and Q_2 predictions also improve for the ACCESS case. On the other hand, the improvement of Q_2 prediction is only 3 % at most with ECHAM, and some simulations perform less well than the

default physics case. The Q_1-error increases more than 50 % by implementing NAM-SCA into ECHAM-SCM.

We interpret that these overall improvements are due to the fact that convection parameterization is clearly required for the GATE case as discussed in Sect. 3. By design, NAM-SCA is physically more consistent than any existing convective parameterizations. The GATE case clearly benefits from the strength of NAM-SCA. However, as a major caveat, it is hard to overwhelmingly beat a performance of a model that already performed well. Clearly, ECHAM-SCM is such a case.

Among all the cases considered, the ECHAM GATE case best establishes superiority of the lowest-resolution model: the case with $\Delta x = 16\,\mathrm{km}$ and $L = 32\,\mathrm{km}$ performs the best in all three error measures. For both Q_1 and Q_2, the error measures continue to increase both with increasing resolutions and domain sizes from this point. Though the error decreases from $\Delta x = 1\,\mathrm{km}$ to $\Delta x = 0.5\,\mathrm{km}$ for L =128–512 km, the decrease is not dramatic and the error never reduces to a level comparable to the lowest-resolution case. The precipitation error also shows a similar tendency except for a more noticeable decrease of the error towards both high resolution ($\Delta x = 0.5\,\mathrm{km}$ with $L \geq 128\,\mathrm{km}$) and large domain ($L = 512\,\mathrm{km}$ with $\Delta x \leq 2\,\mathrm{km}$) limits.

As already emphasized for the stand-alone case, large-domain high-resolution cases do not perform as well for the domain-mean errors in spite of their successful simulations of mesoscale organization. Some examples of time-longitude sections for ECHAM-SCM with NAM-SCA are shown in Fig. 21. Nevertheless, we may note that the propagating features are less organized than the stand-alone cases. Probably, this is due to a lower model top, ECHAM runs do not absorb gravity waves in the sponge layer as much as in the stand-alone runs.

Some examples of the domain-mean precicpitation time series are shown in Fig. 22. Note particularly that the lowest-resolution case (a) is far less noisy than the stand-alone case (cf. Fig. 12a). Even the noisiest case (c) represents better coherencies (the modulation envelope structure) than the stand-alone counterpart (cf. Fig. 12c), though the time series itself is noisier.

The error distributions for the ACCESS GATE case (Fig. 23) is more similar to the stand-alone GATE case than the ECHAM GATE case, except for various details such as the deterio-

ration of Q_1-error by increasing from $L = 32\,\mathrm{km}$ to $64\,\mathrm{km}$ with $\Delta x = 16\,\mathrm{km}$ is not as dramatic as the stand-alone case. Characteristics of the domain-mean precipitation time series with the corresponding resolutions and domain sizes (Fig. 24) are also very similar to the stand-alone cases (cf. Fig. 12).

4.4.3 TWP-ICE case

The TWP-ICE case (Figs. 25, 26) is opposite to the GATE case: the overall model performance in all three error measures worsens by coupling NAM-SCA with the full physics of the GCM-SCMs. Most notably, the errors for Q_1 homogeneously double for ECHAM with all resolution and domain sizes (Fig. 25c). The Q_1 error also increases compared to the default-physics case by up to 80 % for ACCESS (Fig. 26c). Performance with Q_2 is never better than the default-physics case for ACCESS (Fig. 26d), though the overall increase of errors is less dramatic. Performance of precipitation simulation (Figs. 25b, 26b) also deteriorates both for ECHAM and ACCESS compared to the stand-alone cases. In the case for ECHAM, precipitation performs only occasionally better than the default physics, whereas the improvements with ACCESS compared to the default physics may be noted. Note that the performance of the stand-alone case with Q_1 is far better than both with ECHAM and ACCESS, whereas the errors of the stand-alone case with Q_2 are comparable with these cases when either GCM-SCM is implemented. A slight improvement of Q_2 by implementing NAM-SCA into ECHAM-SCM compared to the default physics may be remarked (Fig. 25d).

As already discussed in Sect. 3, convection during TWP-ICE can be considered more directly driven by large-scale processes with less need for convection parameterization. Under this kind of situations, it is likely that consistency of the whole physics (including tunings) becomes more important than consistency of the convection representation itself. For this reason, a straight replacement of NAM-SCA with the default convection parameterization does not contribute much.

Performance of precipitation prediction by ACCESS with NAM-SCA may be worthwhile, because it actually improves overall against the default ACCESS case. However, the comparison with the NAM-SCA stand-alone case shows that the improvement is never better than any

of the stand-alone cases: a model with a "bad" physics can be improved by partially replacing it with a better one, but implementation of "bad" full physics does not necessarily improve a "good" model. Here, the quotation mark is added to the adjective "bad" in order to make it clear that we do not intend to indicate any fundamental defect in ACCESS physics. Rather, simply under the present configuration, the ACCESS physics turns out to be a "bad" combination with NAM-SCA.

4.5 Prediction error

In the analysis so far, we have focused on the errors associated with the convection-related variabilities (precipitation, apparent heat source and moisture sink). Arguably, the purpose of convection parameterization is to make these outputs right in a large-scale model. Thus, this focus appears to be legitimate.

On the other hand, the single-column model inevitably drifts from the climatological state with time as the time integration due to continuous accumulations of small errors. A conventional wisdom may say that this is rather an issue of the consistency of the whole model rather than a problem of convection parameterization par ce. Randall and Cripe (1999) even argue that it is essential to add a relaxation term in order to maintain a climatology in single-column modelling. On the other hand, Emanuel and Zdivkovic-Rothman (1999) strongly argue for the importance of examining the prediction errors rather the source-term errors (Q_1 and Q_2) in order to verify a convection parameterization even under a single-column configuration.

The present section briefly discusses the prediction issues from the latter perspective. More specifically, we examine the RMS prediction errors of the potential temperature and the moisture mixing ratio under the stand-alone configuration and the ECHAM implementation both for GATE and TWP-ICE cases.

The prediction errors for the default ECHAM model are already intriguing. These RMS errors are $1.17\,\mathrm{K}$ and $0.56\,\mathrm{g\,kg^{-1}}$ for the GATE case, and $4.79\,\mathrm{K}$ and $5.25\,\mathrm{g\,kg^{-1}}$ for the TWP-ICE case. Somehow the default ECHAM model has a harder time in predicting the TWP-ICE case correctly in spite of the fact that not much convection parameterization is required as already emphasized in Sect. 3.4. The system becomes warmer and dryer over the simulation

period.

Figures 27 and 28 summarize the RMS errors for the potential temperature and the moisture mixing ratio for the stand-alone NAM-SCA and under implementation into ECHAM, respectively. Here, it may be important to recall that superiority of the small domain, low-resolution case found in analysis of the previous subsections is not that dramatic. These two figures further demonstrate that the accumulations of associated small errors do not necessarily lead to the same conclusion.

The GATE case (a, b) is the most consistent: the case with the smallest domain and the lowest resolution systematically leads to the higher prediction error both for the potential temperature and the moisture. Both for stand-alone and ECHAM cases, the prediction errors tend to decrease when moving towards the larger domains and the higher resolutions. This tendency is very systematic with the ECHAM case (Fig. 28a, b). A general tendency with the TWP-ICE case is far less obvious (Figs. 27 and 28c, d). Nevertheless, the smaller domain and the lowest resolution never gives the best result, not event a local minimum in errors.

Prediction errors turn out to be always higher than the default ECHAM case. We conclude that this is a typical implementation issue that happens when a scheme is tested without tuning. This simple argument is supported by the fact that the stand-alone runs tend to give lower prediction errors than the ECHAM case.

5 Discussions

The present paper reports on a successful implementation of NAM-SCA into the SCMs of two global models (ECHAM, ACCESS). The model has been tested for both the GATE and TWP-ICE cases. A stand-alone SCM configuration is also tested for comparisons.

We found that with reasonable domain size ($L \geq 256\,\mathrm{km}$) and resolution ($\Delta x \leq 2\,\mathrm{km}$), NAM-SCA can simulate the evolution of convective organizations well. However, unfortunately, this capacity does not necessarily contribute to a better prediction of the domain-averaged responses as required for parameterizations.

In fact, a general tendency is that cases with smaller domains and lower resolutions perform

better than cases with larger domains and higher resolutions. This general tendency is confirmed for all the three domain-mean error measures (precipitation, Q_1, Q_2) for all the configurations considered (Figs. 11, 16, 20, 23, 25, 26). The result, against anticipations from physical intuitions (cf. Moncrieff, 1995), suggests that mesoscale convective organization is not a key for parameterizations as long as their goal is limited in prediction of the large-scale variables when the grid-box remains close to the scale of mesoscale organization. Note that the importance of mesoscale organization, for example, for successfully predicting convective-scale precipitation would be another issue.

More specifically, a two-column configuration with a relatively low resolution, $\Delta x = 8$–$16\,\mathrm{km}$, and a relatively small domain size, $L = 32$–$68\,\mathrm{km}$, tends to perform the best. This result suggests that one degree of freedom with a bulk mass-flux parameterization is sufficient in order to construct a parameterization with satisfactory performance. In other words, this result suggests that lack of complexity is probably not the main problem of the current convection parameterizations, though many processes are still missing in their formulations. Thus, a relatively simple formulation should be able to construct a reliable parameteization so long as it is physically consistent (cf. Yano et al., 2005).

Though lack of mesoscale organization is often cited as a major defect of the current convection parameterizations, the present study suggests this is not necessarily the case. Though a sufficiently large domain and a sufficiently high resolution may be required for successfully simulating these organizations, such information is not necessarily required if the goal is solely to obtain proper grid-box mean convective responses. Only the latter is the goal of convection parameterization. It may, however, be emphasized that the convective momentum transport is not considered in the present study. This is a particular aspect where the mesoscale convective organization may play an important role (Moncrieff, 1992; Yano and Moncrieff, 1998).

Our preliminary investigations suggest that for a large domain with a high resolution to outperform a low-resolution small-domain run, then at least $\Delta x \leq 0.5\,\mathrm{km}$ and $L \geq 256\,\mathrm{km}$ are required. In order to see this tendency more clearly, experiments with larger domains and higher resolutions would be required. Note that the present experiments are limited to $\Delta x \geq 0.5\,\mathrm{km}$ and $L \leq 512\,\mathrm{km}$.

However, it is also emphasized that superiority of the small domain, low-resolution case is not that dramatic. Moreover, in the GATE case, the small domain, low-resolution run suffers from a strong moistening tendency in the boundary layer, partially due to a lack of proper interactions between convection and the boundary-layer processes under the present configuration. As a result, when the prediction errors are instead taken as a model performance measure for the GATE case, a clear monotonic tendency is found that the large domain, high-resolution case performs the best and the small domain, small-resolution case performs the worst.

As a whole, it is likely that a relatively poor performance of NAM-SCA coupled to the GCM physics is partially due to the fact that various interactions with convection by the other subgrid-scale processes are not properly considered by the current model configuration. We especially speculate that interferences of NAM-SCA with the boundary layer scheme could be an issue. Under the current set-up, the boundary-layer tendencies are given only in terms of the domain mean. As a result, the boundary-layer processes, for example, does not see a presence of a cold pool generated by NAM-SCA within a boundary layer. Thus, it does not lead to enhancement of surface fluxes as expected.

In the present study, we did not attempt a brutal implementation of a GCM boundary-layer package into NAM-SCA. Rather our goal would be to develop a minimum boundary-layer scheme necessary for subgrid-scale parameterizations, as we have already attempted for the microphysics (Yano and Bouniol, 2010, 2011).

On the other hand, the often-best performance of the lowest-resolution case is likely not totally due to the lack of complete physical interactions in the subgrid-scales under the present model configuration. Remarkably, even under an implementation of full CRMs (conventional super-parameterization), it is reported that a relatively low-resolution with a small domain is sufficient for obtaining a consistent global model performance: a two-dimensional CRM only with 8-columns has worked equally well as the standard choice with 64-columns (Khairoutdinov et al., 2005). The present work suggests, based on the obtained quantitative error measures, that it is possible to push the truncation further.

The above result further suggests that a simple subdivision of a grid box domain with a relatively limited number of subdomains could work better than conventional parameterizations

for representing subgrid-scale convective processes based on a parametric procedure. It may be worthwhile to recall that Yano et al. (2005), and Yano et al. (2010) interpret the basic starting point of mass-flux parameterization as such a subdivision of the grid box. Their analysis further suggests that subgrid-scale parameterization may better be re-interpreted as an issue of mesh refinement (Yano et al., 2010; Yano, 2010). Alternatively, the issues of convection parameterization may be, to a good extent, circumvented simply by increasing the horizontal resolution of a global or a regional model only to a modest level (20–50 km). For example, Knutson et al. (2007), Garner et al. (2009), Zhao et al. (2009) suggest that such a resolution is good enough for successfully simulating tropical cyclones.

In conclusion, NAM-SCA is successfully implemented into SCM versions of operational GCMs. The various theoretical issues behind in the subgrid-scale parameterizations are elucidated under this implementation exercise. Our next goal is clearly to implement NAM-SCA into a full three-dimensional version of GCM. Improvement of the compression rate of the model is also an important priority.

The present studies show that the compression rate linearly improves both with logarithmically increasing resolutions and domain sizes: no compression in the two-segment limit (by design) to the rate close to 0.1 at $\Delta x = 0.5\,\mathrm{km}$ and $L \geq 256\,\mathrm{km}$. In this respect, our main challenge would be to develop an advanced version of NAM-SCA that permits much higher truncation rates, even down to two to three segments, but with much more flexible distribution of segments both in terms of their sizes and spatial distributions. Such a configuration would greatly improve the performance of our two-segment runs, but with an equivalent computational cost.

Strictly, the concept of compression is not limited to the total number of active finite volumes. The same concept must more importantly be applied to the physics of the model, notably for cloud microphysics. The latter is so involved and complex that from a point of view of genius cloud microphysics, any simplifications may even appear to be totally forbidden. However, not all the microphysical–scale details clearly influence all the larger scales, as already suggested by Seifert et al. (2012). Under this spirit, we emphasize the importance of implementing only the minimum, necessary physics as subgrid-scale processes. However, extensive research is still

required in order to identify a methodology itself that is required in order to objectively define such absolute minimum, necessary physics under a given large–scale state.

Appendix A Model parameters

Here, the model parameters are listed with the values adopted. See Yano et al. (2010) for the precise definitions of the parameters.

A1 Model resolution related parameters

$L = 32 - -512$ km:	horizontal domain size
$N_x = 2 - -1024$:	total number of mesh segments under a full resolution
$M_x = 2$:	minimum number of mesh segments allowed at each vertical level
$\Delta t = 5$ s:	time step: default
2 s:	N_x = 256–1024, $\Delta x = 0.5\,\mathrm{km}$; additionally with N_x = 512, $\Delta x = 1\,\mathrm{km}$; N_x = 64–512, $\Delta x = 0.5\,\mathrm{km}$ for ACCESS.
1 s:	ACCESS, N_x = 512–1024, $\Delta x = 0.5\,\mathrm{km}$
$\Delta X = L/2$:	length of the mesh segment under the minimum resolution
$\Delta x = 0.5 - -16$ km:	full horizontal resolution

A2 Vertical coordinate

H = 50 km:	model top-height: stand-alone cases
30 km:	ECHAM (GCM top level)
35 km:	ACCESS (GCM top level)
$N_z = 51$:	total number of full vertical levels: stand-alone case
38:	GCM-SCM
$\Delta z_0 = 50$ m:	the highest vertical resolution at the lowest layer (full-level layer detph): stand alone cases
80 m:	ECHAM
20 m:	ACCESS
$\Delta z_n = 1000$ m:	the lowest vertical resolution (full-level layer depth): stand-alone cases, ECHAM
3600 m:	ACCESS (identical to the ACCESS' lowest resolution at the top)
$z_{1,\mathrm{R}} = 15$ km:	the bottom of the sponge layer: stand-alone cases, ACCESS
25 km:	ECHAM
$z_{2,\mathrm{R}} = 30$ km:	the level above which the maximum Rayleigh damping rate is imposed: stand-alone cases
27 km:	ECHAM
25 km:	ACCESS
$\tau_{\mathrm{R}} = 120$ s:	the maximum Rayleigh damping time-scalein the sponge layer

A3 Critical vertical levels

$k_b = 1$:	maximum height at which the full resolution is always maintained
$k_m = 40$:	top height at that the full resolution is initially introduced
$k_t = N_z$:	maximum height level at which activation and deactivation of mesh segments is performed. Above this level, the minimum resolution M_x is always maintained

A4 Vertical depth for performing activation and deactivation

$\Delta k_{\mathrm{a}} = 3$: vertical depth over which activation is performed
$\Delta k_{\mathrm{d}} = 0$: vertical depth over which the deactivation condition is checked

A5 Intervals for activation and deactivation

$n_{\mathrm{a}} = 10$: interval for performing activation given as a number of time steps
$n_{\mathrm{d}} = 10$: interval for performing deactivation given as a number of time steps

A6 Relative thresholds for activation and deactivation

$\gamma_{\mathrm{a}} = 1.0$: threshold for activation relative to the standard deviation at a given vertical level
$\gamma_{\mathrm{d}} = 1.0$: threshold for deactivation relative to the standard deviation at a given vertical level
$\gamma_{\mathrm{min}} = 0.1$: threshold for activation and deactivation relative to the total standard deviation

Appendix B ECHAM Physics

The ECHAM physics are reviewed by Stevens, et al (2013).

B1 Convection

A bulk mass–flux scheme originally developed by Tiedtke (1989) is used for moist convection parameterization. The current scheme includes shallow and midlevel convection in addition to deep convection, but with only one convection type allowed at any given time. A preference is given to deep convection. A component for deep convection is revised by Nordeng (1994), whereas shallow and midlevel convection uses the original Tiedtke formulation.

Closure is based on convective available potential energy (CAPE) for deep convection, whereas moisture closure is adopted for shallow convection. Details are discussed in Möbis and Stevens (2013).

B2 Clouds

The cloud fraction is evaluated by a simple diagnostic formulation depending on the grid–point relative humidity as proposed by Sundqvist et al (1989, see their Eq. 3.13). A critical relative humidity, a free parameter of the formulation, is adjusted based on a cloud–resolving model study by Xu and Kruger (1991).

B3 Cloud Microphysics

Large–scale cloud microphysics are described by a single-moment bulk scheme (Lohmann and Roeckner 1996). The scheme considers the three types of water: vapour, liquid, ice. Warm microphysics formulation is basically taken from Beheng (1994) double–moment formulation, but it is simplified by assuming prescribed cloud and rain number concentrations by environment. Ice physics are developed strictly in bulk manner by assuming an exponential size distribution (Gunn and Marshall 1958). Large–scale precipitation is treated diagnostically given the conversion terms from the prognostically–described water phases. Detrainment of hydrometeors from parameterized convection is also taken into account.

B4 Convective Precipitation (Johannes Quaas, personal communication, March 2011: ”Convection microphysics in ECHAM6”, http://convection.zmaw.de/Discussion-Documents.1851.0.html)

Convective precipitation rate is assumed to be proportional to the cloud water content, l:

$$K(p)l$$

The proportionality, $K(p)$, is defined by

$$K(p) = \begin{cases} K_c & \text{if } p_B - p \geq p_0 \\ 0 & \text{otherwise} \end{cases}$$

with p_B the cloud base pressure; $p_0 = 150$ hPa over ocean and $p_0 = 300$ hPa over land. A resolution dependent constant is here set $K_c = 10^{-4}$. ECHAM also consider re–evaporation of precipitation water below the cloud base.

B5 Other physics

The boundary–layer scheme is based on a 1.5–order closure in moment expansion with the turbulent kinetic energy (TKE) computed prognostically in order to define a eddy diffusion coefficient (Brinkop and Roeckner 1995). Dependence of the eddy diffusion on TKE mimics the cloud-top entrainment.

Radiation calculation is based on a two–stream formulation by Iacono et al (2008). Maximum–random cloud overlap (cf., Geleyn and Hollingworth 1979) is assumed for considering the radiative–cloud interactions.

Appendix C ACCESS–SCM Physics

The ACCESS SCM used in the present study is based on the Australian Parallel Suite 1 (APS1) ACCESS-G model, which is based on UKMO UM7.5. Details on APS1 are described in the NMOC Operations Bulletin Number 93, relating to APS1 upgrade of the ACCESS-G Numerical Weather Prediction system, which was released in November 2012 and is available at http://www.bom.gov.au/australia/charts/bulletins/nmoc_bulletin.shtml.

C1 Convection

A modified version of bulk mass–flux scheme originally developed by Gregory and Rowntree (1990) is adopted for moist convection parametrization. For deep convection, the cloud-base

mass-flux is calculated based on the reduction of convective available potential energy (CAPE) to zero over a given timescale. The CAPE closure has been modified in various ways to enhance model stability, with the vertical-velocity-based CAPE closure used. Under this framework, if the maximum large-scale vertical velocity, evaluated before convection, is larger than the threshold vertical velocity, the CAPE timescale is reduced in order to remove the convective instability more rapidly.

C2 Clouds

The cloud fraction is computed prognostically with the prognostic cloud and condensate (PC2) scheme (Wilson et al., 2008). Under this scheme, fractions for liquid clouds and ice clouds are computed separately, but no mixed–phase cloud is considered. These two values are passed on to radiative transfer computations. In NAM–SCA implementation of ACCESS, these two cloud fraction values are replaced by those diagnosed from NAM–SCA as described in the main text.

PC2 provides a comprehensive framework for cloud descriptions by fully coupling it with cloud microphysics as well as by taking into account of the other processes such as detrained cloud water from convection, radiation, and boundary layer processes.

C3 Cloud Microphysics

Large–scale cloud microphysics (Wilson and Ballard 1999) are described by a single-moment bulk scheme, overall based on Rutledge and Hobbs (1983). The scheme considers the three types of water: vapour, liquid, ice. A single ice water prognostic variable is further split by a diagnostic relationship into ice crystals and aggregates, which are treated separately in the microphysical conversion terms before being recombined after the calculations. The microphysical processes calculated in the scheme are: sedimentation of ice and rain, heterogeneous and homogeneous nucleation of ice particles, deposition and sublimation of ice, aggregation, riming and melting of ice, collection of cloud droplets by raindrops, autoconversion and accretion production of raindrops, and evaporation of rain (condensation and evaporation of cloud water is performed by the cloud scheme).

C4 Convective Precipitation (Rachel Stratton, personal communication, March 2011)

When the cloud water/ice, l, within convection exceeds a minimum value, l_{min}, convection begins to precipitate, and it is given by

$$(l - l_{min})\frac{M}{g}$$

Here, M is the convective mass flux, g is the acceleration of the gravity. A height–dependent minimum (kg/kg) is defined over ocean by

$$l_{min} = \min(10^{-3}[2 + 0.5\tanh(\frac{1500 - h_c}{1000})], 0.5q^*)$$

where h_c is the cloud depth at a given level, q^* is the saturation specific humidity of the environment. The above value is multiplied by two over land; l_{min} is also limited to the range between 2×10^{-5} kg/kg and 3×10^{-4} kg/kg.

C5 Other physics

The boundary–layer scheme, as described by Lock et al. (2000) and updated by Brown et al. (2008), is an eddy–diffusion based approach with a vertical profile of the eddy–diffusion coefficient prescribed based on an environmental state (stable or unstable, etc). This procedure mimics "non–local" transport. The scheme also includes an explicit entrainment parameterization at the boundary–layer top.

Radiation calculation is based on two–stream approximation described by Edwards and Slingo (1996). Maximum–random cloud overlap (cf., Geleyn and Hollingworth 1979) is assumed for considering the radiative–cloud interactions.

Appendix D Comparison of the two default SCM physics

D1 Convection

Both models use a bulk mass–flux scheme with a CAPE closure as a default. However, they are different in details including the treatments of closure and entrainment–detrainment rates.

D2 Clouds

For cloud fraction evaluation, ECHAM adopts a simple diagnostic formula (Sundqvist et al 1989), whereas ACCESS adopts an extremely elaborated PC2 scheme which contains extensive coupling with various physical processes (Wilson et al., 2008). The latter also compute the liquid and the ice cloud fractions separately. However, a careful examination of the latter formulation casts a doubt whether such an elaboration is an advantage.

D3 Cloud microphysics

Though different in details of flavors, both models adopts the cloud microphysics descriptions with a comparable level of complexity.

D4 Other physics

Both boundary–layer schemes are based on the idea of eddy diffusion. However, they take substantially different strategies in detail. ECHAM (Brinkop and Roeckner 1995) takes a 1.5–order closure, but strictly remains with local descriptions. On the other hand, ACCESS technically stays with a first–order closure, but overcomes its limitation by introducing a "non–local" dependence on the eddy–diffusion coefficient.

Both models assume two–stream approximation for the radiative–transfer calculations with a same level of complexity in details. Both models assume the maximum–random cloud overlap (cf., Geleyn and Hollingworth 1979).

Acknowledgements. Discussions with Marco Georgetta, Johannes Quaas on ECHAM with Vaughan Barras, Zhian Sun, Hongyan Zhu on ACCESS are greatly appreciated. The first author's visitorships were enabled by supports by BoM, CNRS, and MPI. The present work is performed under a framework of COST Action ES0905.

The publication of this article is financed by CNRS-INSU.

References

Aspliden, C. L.: A classification of the structure of the tropical atmosphere and related energy fluxes, J. Appl. Meteorol., 15, 692–697, 1976.

Bender, C. M. and Orszag, S. A.: Advanced Mathematical Methods for Scientists and Engineers, McGraw-Hill, New York, 593 pp., 1978.

Cox, S. K. and Griffith, K. T.: Estimates of radiative divergence during phase III of the GARP Atlantic tropical experiment. Part II: analysis of Phase II results. J. Atmos. Sci., 46, 1566–601, 1979.

Emanuel, K. A. and Zdivkovic-Rothman, M.: Development and evaluation of a convection scheme for use in climate models. J. Atmos. Sci., 56, 1766–1782, 1999.

Esbensen, S. K., Tollerud, E. I., Chu, J.-H.: Cloud-cluster-scale circulations and the vorticity budget of synoptic-scale waves over the Eastern Atlantic intertropical convergence zone, Mon. Wea. Rev., 110, 1677–1693, 1982.

Fraedrich, K. and McBride, J. L.: The physical mechanism of CISK and the free-ride balance, J. Atmos. Sci., 46, 2642–2648, 1989.

Garner, S., Held, I., Knutson, T., and Sirutis, J.: The roles of wind shear and thermal stratification in past and projected changes of Atlantic tropical cyclone activity, J. Climate, 22, 4723–4734, 2009.

Grabowski, W. W.: Towards cloud resolving modelling of large-scale tropical circulations: a simple cloud microphysics parameterization, J. Atmos. Sci., 55, 3283–3298, 1998.

Grabowski, W. W., and Smolarkiewicz, P. K.,: CRCP: a cloud resolving convection parameterization for modeling the tropical convective atmosphere, Physica D, 133, 171–178, 1999.

Grabowski, W. W., Wu, X., and Moncrieff, M. W.: Cloud-resolving modeling of tropical cloud systems during Phase II of GAT E. Part I: Two-dimensional experiments, J. Atmos. Sci., 53, 3684–3709, 1996.

Houze Jr., R. A. and Betts, A. K.: Convection in GATE, Rev. Geophys. Space Phys., 19, 541–576, 1981.

Hudlow, M. D. and Patterson, V. L.: GATE radar rainfall atlas, NOAA special Report, US Govt. Printing Office, Washington DC, 155 pp., 1979.

Khairoutdinov, M., Randall, D., and DeMott, C.: Simulations of the atmospheric general cirrulcation using a cloud-resolving model as a superparameterization of physical processes, J. Atmos. Sci., 62, 2136–2154, 2005.

Kiehl, J. T., Hack, J. J., and Briegleb, B. P.: The simulated Earth radiation budget of the national center for atmospheric research community climate model CCM2 and comparisons with the Earth radiation budget experiment (ERBE), J. Geophys. Res., 99, 20815–20827, 1994.

Knutson, T. R., Sirutis, J. J., Garner, S. T., Held, I. M., and Tuleya, R. E.: Simulation of the recent multi-decadal increase of Atlantic hurricane activity using an 18-km-grid regional model, B. Am. Meteorol. Soc., 88, 1549–1565, 2007.

May, P. T., Mather, J. H., Vaughan, G., and Jacob, C.: Characterizing oceanic convective cloud systems: the tropical warm pool international cloud experiments, B. Am. Meteorol. Soc., 154, 153–155, 2008.

Marshall, J. S. and Palmer, W. M.: The distribution of raindrops with size, J. Meteorol., 5, 165–166, 1948.

Moncrieff, M. W.: Organized convective systems – archetypal dynamic-models, mass and momentum flux theory, and parametrization, Q. J. Roy. Meteorol. Soc., 507, 819–850, 1992.

Moncrieff, M. W.: Mesoscale convection from a large–scale perspective, Atmos. Res., 35, 87–112, 1995.

Pedlosky, J.: Geophysical Fluid Dynamics, 2nd edn., 710 pp., Springer-Verlag, New York, USA, 1987.

Pruppacher, H. R. and Klett, J. D.: Microphysics of Clouds and Precipitation, 2nd revised and enlarged edition with an introduction to cloud chemistry and cloud electricity, Kluwer Academic Publisheres, Dordrecht, The Netherlands, 954 pp., 1997.

Rogers, R. R. and Yau, M. K.: Short Course in Cloud Physics, 3rd edn., Pergamon Press, 290 pp., Oxford, England, 1989.

Randall, D. A. and Cripe, D. G.: Alternative methods for specification of observed forcing in single-column models and cloud system models. J. Geophys. Res., 104, 24527–24545, doi:10.1029/1999JD900765, 1999.

Randall, D. A., Khairoutdinov, M., Arakawa, A., and Grabowski, W.: Breaking the cloud parameterization deadlock, B. Am. Meteorol. Soc., 84, 1547–1564, 2003.

Riehl, H. and Malkus, J. S.: On the heat balance in the equatorial trough zone, Geophysica 6, 503–538, 1958.

Seifert, A., Köhler, C., and Beheng, K. D.: Aerosol-cloud-precipitation effects over Germany as simulated by a convective-scale numerical weather prediction model, Atmos. Chem. Phys.12, 709-725, 2012

Sobel, A. H., Nilsson, J., and Polvani, L. M.: The weak temperature gradient approximation and balanced tropical moisture waves, J. Atmos. Sci., 58, 3650–3665, 2001.

Sui, C.-H. and Yanai, M.: Cumulus ensemble effects on the large–scale vorticity and momentum fields of GATE. Part I: observational evidence, J. Atmos. Sci., 43, 1618–1642, 1986.

Thompson Jr., R. M., Payne, S. W., Recker, E. E., and Reed, R. J.: Structure and properties of synoptic–scale wave disturbances in the intertropical convergence zone of Eastern Atlantic, J. Atmos. Sci., 36, 53–72, 1979.

Varble, A., Fridlind, A. M., Zipser, E. J., Ackerman, A. S., Chaboureau, J.-P., Fan, J., Hill, A., McFarlane, S. A., Pinty, J.-P., and Shipway, B.: Evaluation of cloud-resolving model intercomparison simulations using TWP-ICE observations: precipitation and cloud structure, J. Geophys. Res., 116, D12206, doi:10.1029/2010JD015180, 2011.

Wapkler, K., Lane, T. P., May, P. T., Jacob, C., Manton, M. J., and Siems, S. T.: Cloud–system–resolving model simulations of tropical cloud systems observed during the tropical warm pool-international cloud experiment, Mon. Weather Rev., 138, 55–73, 2010.

Xie, S., Hume, T., Jacob, C., Klein, S. A., McCoy, R. B., and Zhang, M.: Observed large-scale structure and diabatic heating and drying profiles during TWP-ICE, J. Climate, 23, 57–79, 2010.

Xu, K.- M. and Randall, D. A.: Explicit simulation of cumulus ensembles with the GATE Phase III data: comparison with observations, J. Atmos. Sci., 53, 3710–3736, 1996.

Yanai, M. S., Esbensen, S., and Chu, J. H.: Determination of bulk properties of tropical cloud clusters from large-scale heat and moisture budgets, J. Atmos. Sci., 30, 611–627, 1973.

Yano, J. I.: Residual cumulus parameterization, Q. J. Roy. Meteorol. Soc.,127, 1261–1276, 2001.

Yano, J.-I.: Deep-convective vertical transport: what is mass flux?, Atmos. Chem. Phys. Discuss., 9, 3535–3553, doi:10.5194/acpd-9-3535-2009, 2009.

Yano, J. I.: Downscaling, parameterization, decomposition, compression: a perspective from the multiresolutional analysis, Adv. Geophys., 23, 65–71, 2010.

Yano, J.-I. and Bouniol, D.: A minimum bulk microphysics, Atmos. Chem. Phys. Discuss., 10, 30305–30345, doi:10.5194/acpd-10-30305-2010, 2010.

Yano, J.-I. and Bouniol, D.: Interactive comment on "A minimum bulk microphysics" by J.-I. Yano and D. Bouniol., Atmos. Chem. Phys. Discuss., 10, C14638–C14654, avaiable at: www.atmos-chem-phys-discuss.net/10/C14638/2011/., last access: March 2011, 2011.

Yano, J.-I. and Moncrieff, M. W.: The impact of mesoscale momentum transport on the large-scale tropical circulation: a linear analysis J. Atmos. Sci., 55, 1038–1050, 1998.

Yano, J.-I., Moncrieff, M. W., and McWilliams, J. C.: Linear stability and single–column analyses of several cumulus parameterization categories in a shallow–water model, Q. J. Roy. Meteorol. Soc., 124, 983–1005, 1998.

Yano, J.-I., Benard, P., Couvreux, F., and Lahellec, A.: NAM-SCA: nonhydrostatic anelastic model under segmentally-constant approximation, Mon. Weather Rev., 138, 1957–1974, 2010.

Yano, J.-I., Bechtold, P., Redelsperger, J.-L., and Guichard, F.: Wavelet-compressed representation of deep moist convection, Mon. Weather Rev. 132, 1472–1486, 2004.

Yano, J.-I., Redelsperger, J.-L., Guichard, F., and Bechtold, P.: Mode decomposition as a methodology for developing convective-scale representations in global models, Q. J. Roy. Meteorol. Soc.,131, 2313–2336, 2005.

Zhao, M., Held, I. M., Lin, S.-J., and Vecchi, G. A.: Simulations of global hurricane climatology, interannual variability, and response to global warming using a 50-km resolution GCM., J. Climate, 22, 6653–6678, 2009.

Zipser, E. J.: Mesoscale and convective-scale downdrafts as distinct components of squall-line structure, Mon. Weather Rev., 105, 1568–1589, 1977.

Table 1. A list of the models used in the present study. It consists of a combination of a subrid-scale model (left column) and a host model (SCM: first row). Section numbers are given where the given model combinations are considered.

		GCM-SCM	
Sub-Grid\SCM	Stand-Alone	ECHAM	ACCESS
NAM-SCA	Sect. 4.2, 4.3	Sect. 4.4	Sect. 4.4
default physics	–	Sect. 4.1	Sect. 4.1

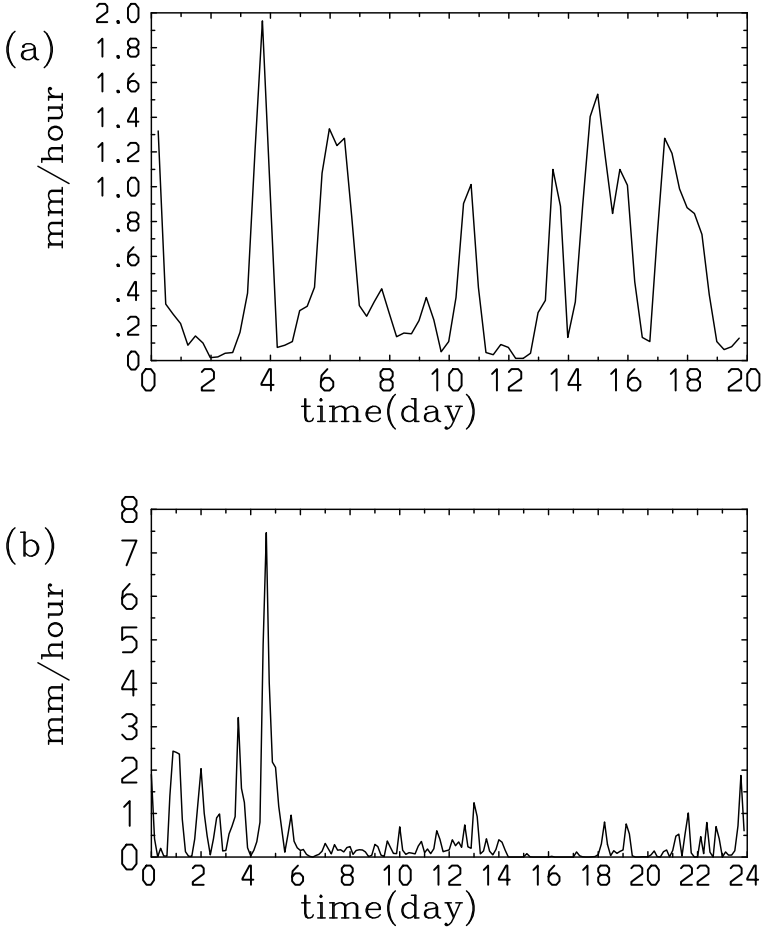

Fig. 1. The observed time series during **(a)** the GATE Phase III and **(b)** the TWP–ICE periods.

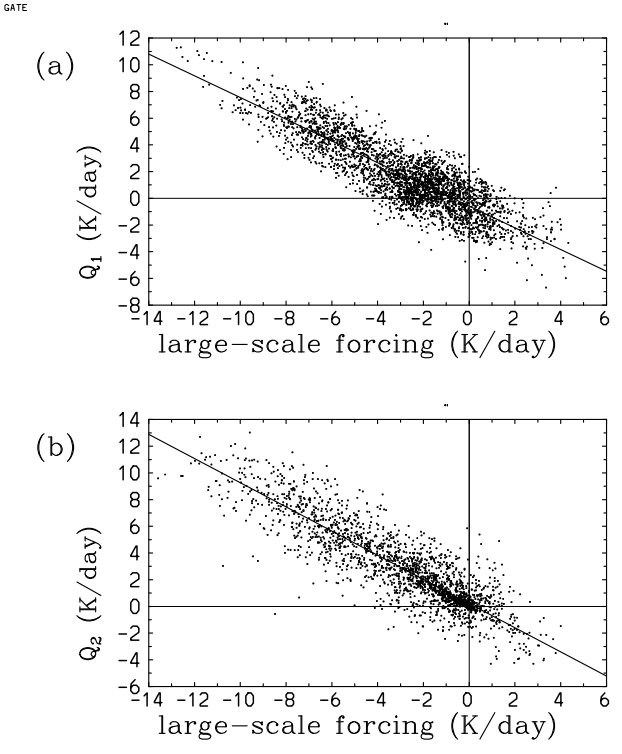

Fig. 2. Scatter plot between the large-scale forcing, $\bar{F}_{\rm L}$ and the apparent source Q for the static energy (potential temperature: **(a)**) and the water vapor **(b)** for the GATE case. The water-vapor budget is defined in terms of sink with positive sign corresponding to a decrease of water vapor. Data available for all the vertical levels is plotted for the whole period of the case. Furthermore straight lines with least-square fits are added in order to indicate the degree that the tendencies satisfy the "free ride" principle. The slopes for the least-square fits are -0.86 and -0.90 in **(a)** and **(b)**, respectively.

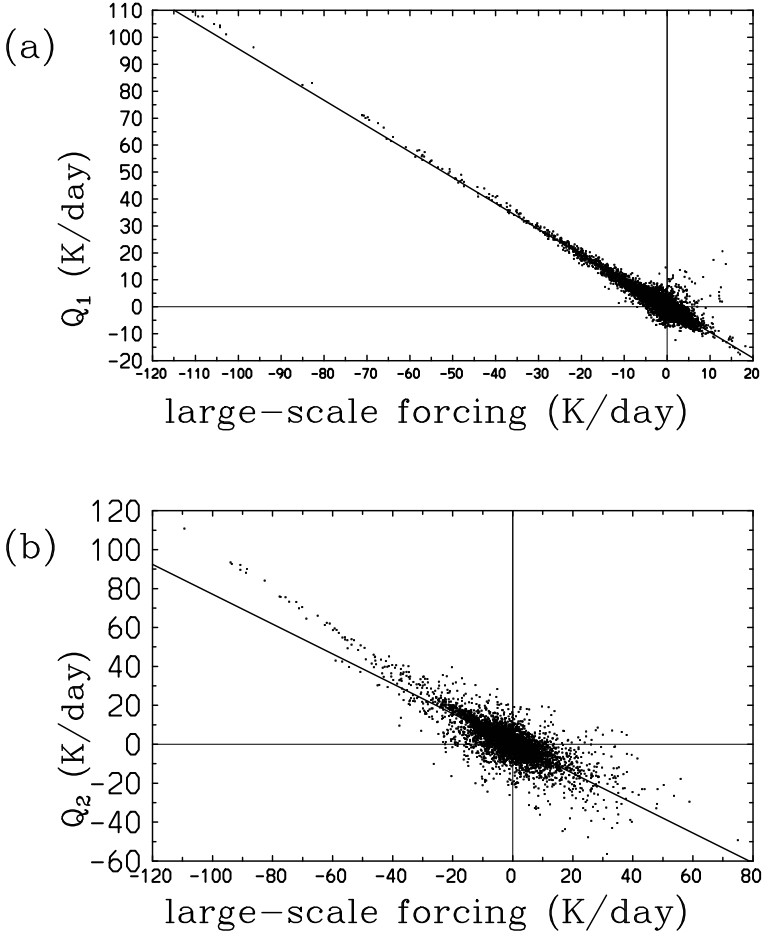

Fig. 3. The same as Fig. 2 but for the TWP-ICE case. The slopes with least-square fits are −0.94 and −0.74 in **(a)** and **(b)**, respectively.

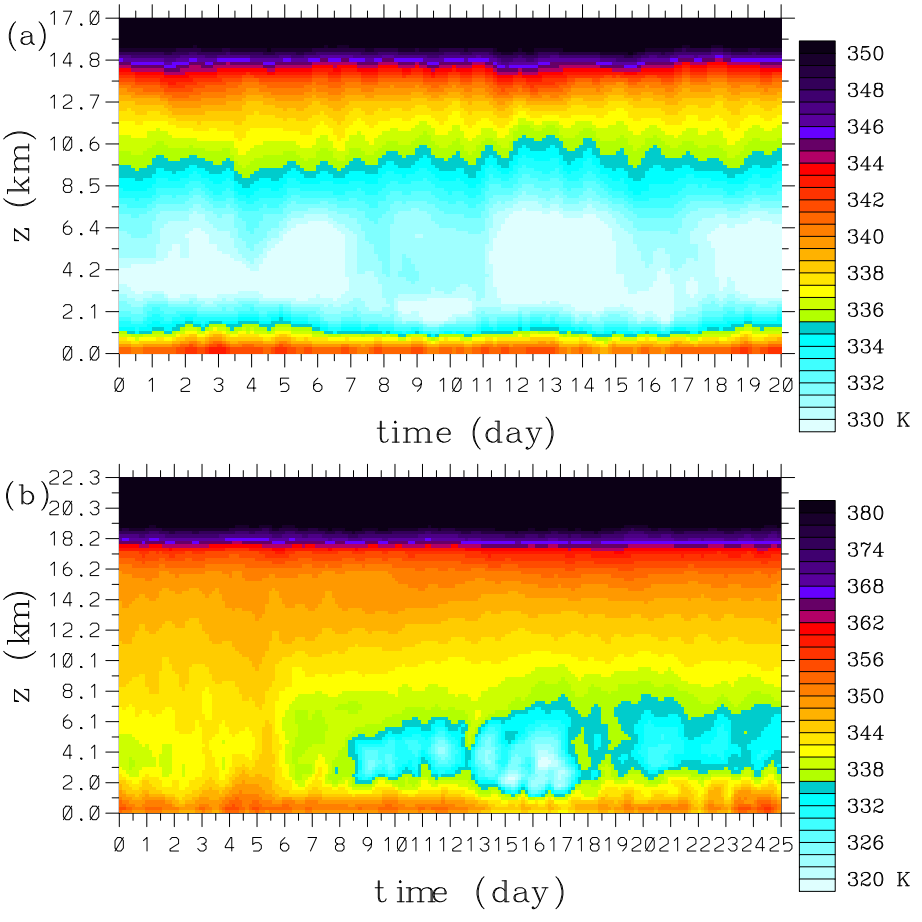

Fig. 4. Time-height section of moist static energy for **(a)** GATE Phase III and **(b)** TWP-ICE periods. Here, the plots are made by dividing the quantity by the specific heat at constant pressure so that is it given in the unit of temperature (K).

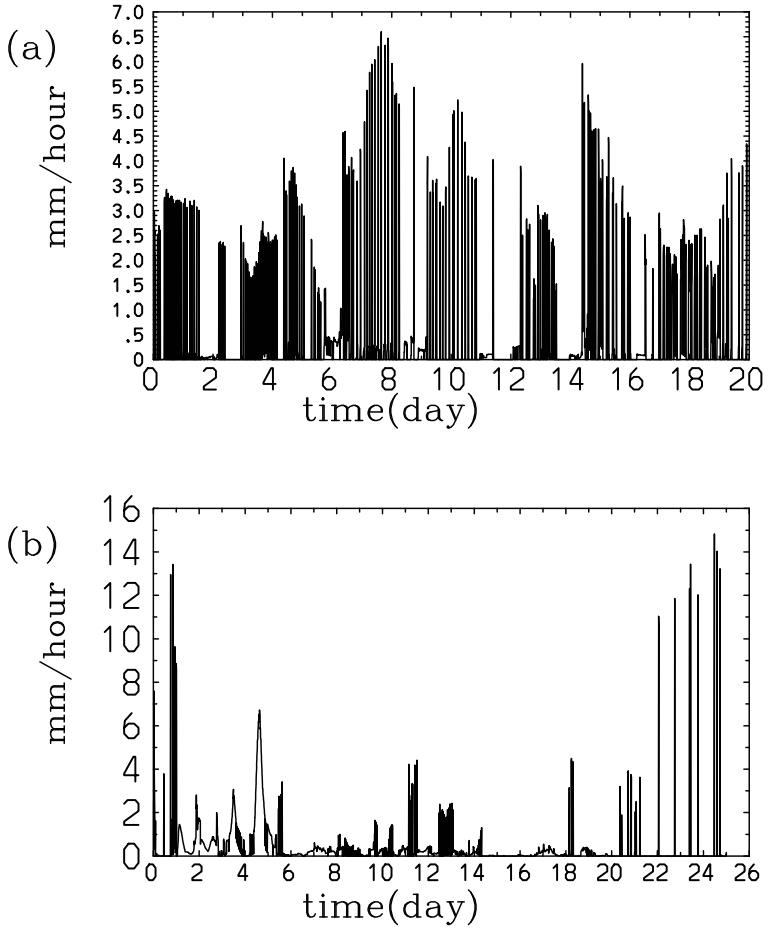

Fig. 5. The precipitation time series simulated by ECHAM-SCM with default physics for **(a)** the GATE Phase III and **(b)** the TWP–ICE periods. Plots use outputs averaged over every 1 h and 3 h, respectively.

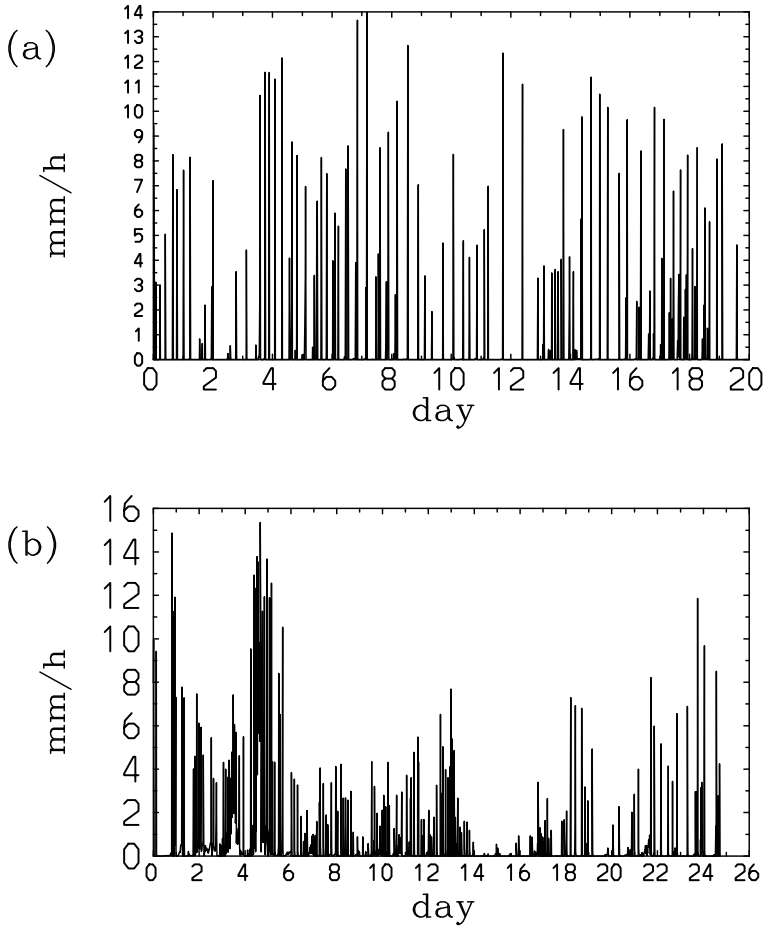

Fig. 6. The precipitation time series simulated by ACCESS-SCM with default physics for **(a)** the GATE Phase III and **(b)** the TWP-ICE periods. Here, data is plotted for every time step.

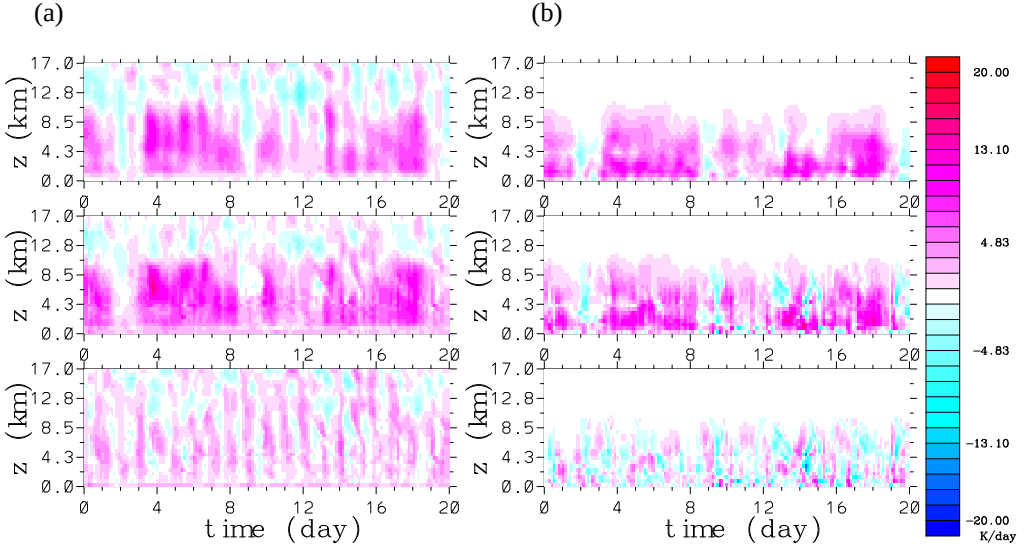

Fig. 7. The time-height section of apparent heat source, Q_1 **(a)**, and apparent moisture sink, Q_2 **(b)** for the GATE Phase III period from (top) observations, (middle) as simulated by ECHAM-SCM default physics and (bottom) the difference.

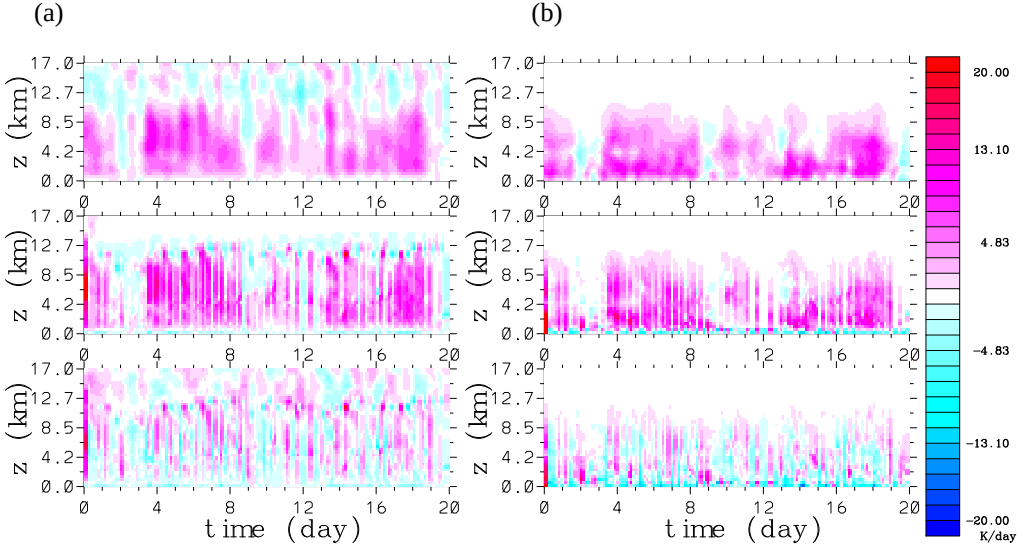

Fig. 8. The time-height section of apparent heat source, Q_1 **(a)**, and apparent moisture sink, Q_2 **(b)** for the GATE Phase III period from (top) observations, (middle) as simulated by ACCESS-SCM default physics and (bottom) the difference.

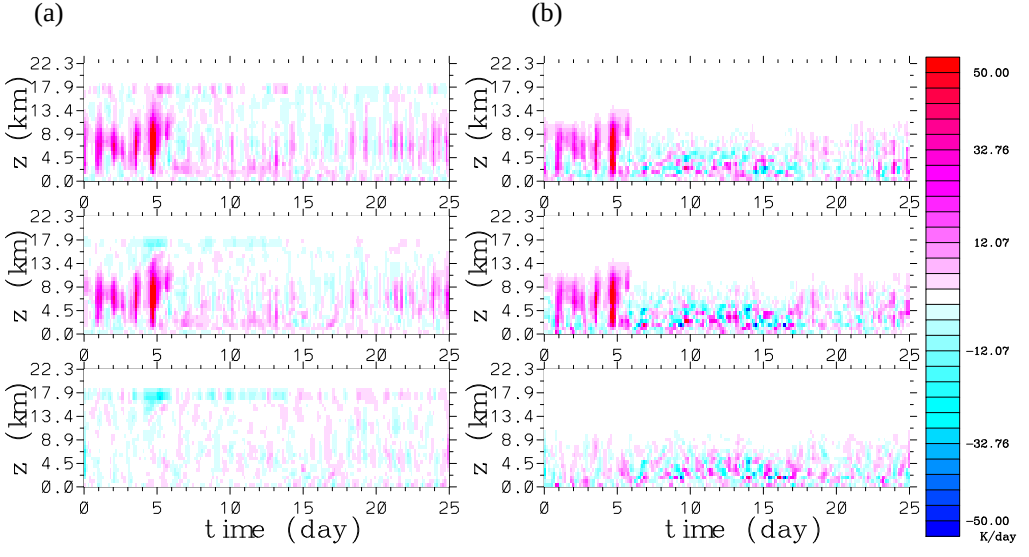

Fig. 9. The time-height section of apparent heat source, Q_1 **(a)**, and apparent moisture sink, Q_2 **(b)** for the TWP-ICE period from (top) observations, (middle) as simulated by ECHAM-SCM default physics and (bottom) the difference.

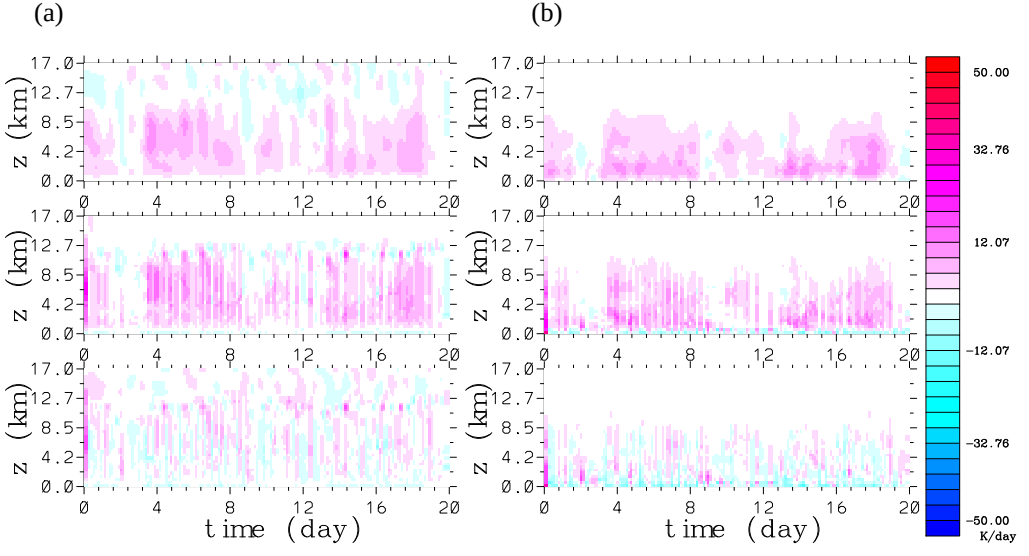

Fig. 10. The time-height section of apparent heat source, Q_1 (left), and apparent moisture sink, Q_2 (left) for the TWP-ICE period from (top) observations, (middle) as simulated by ACCESS-SCM default physics and (bottom) the difference.

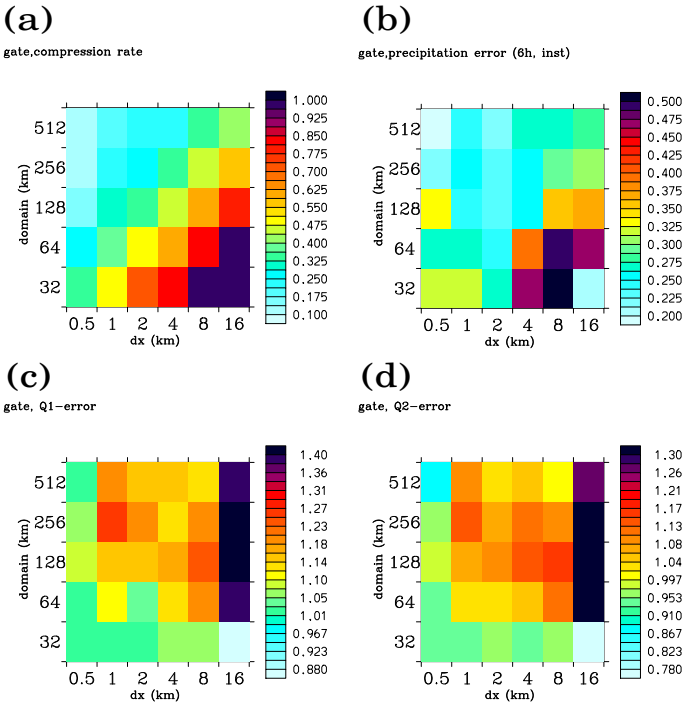

Fig. 11. Summary of stand-alone GATE case: **(a)** compression rate, along with the normalized RMS errors for **(b)** precipitation, **(c)** Q_1, and **(d)** Q_2 shown as function of the horizontal resolution, Δx (horizontal axis) and the domain size, L (vertical axis). Errors are normalized against the ACCESS default cases.

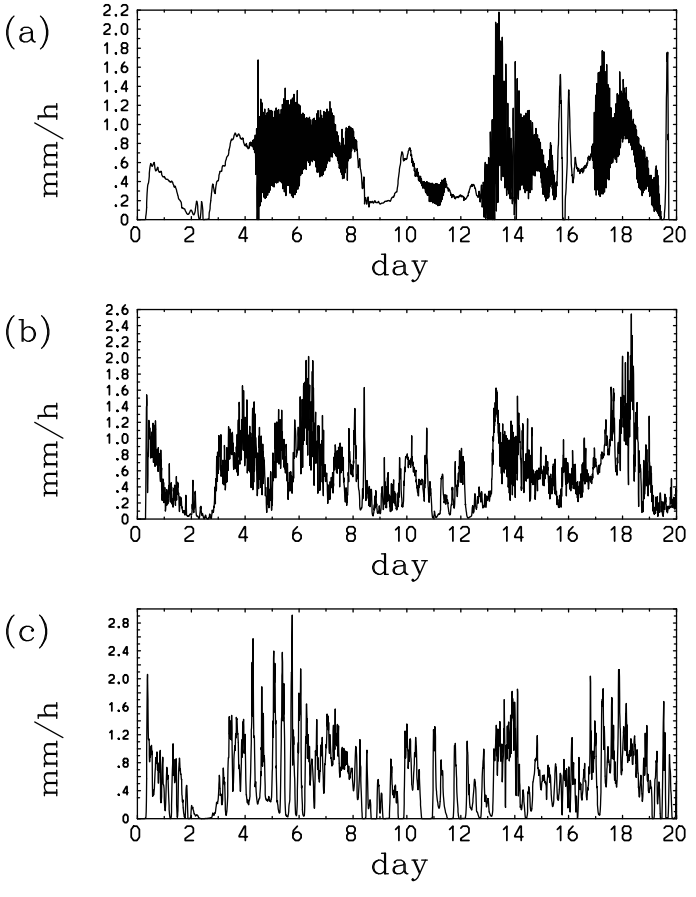

Fig. 12. The domain-mean precipitation time series during the GATE Phase III period obtained by stand-alone simulations: **(a)** $\Delta x = 16\,\mathrm{km}$, $L = 32\,\mathrm{km}$, **(b)** $\Delta x = 0.5\,\mathrm{km}$, $L = 512\,\mathrm{km}$, **(c)** $\Delta x = 4\,\mathrm{km}$, $L = 256\,\mathrm{km}$. Note that the precipitation rate is plotted for every $10\,\mathrm{min}$.

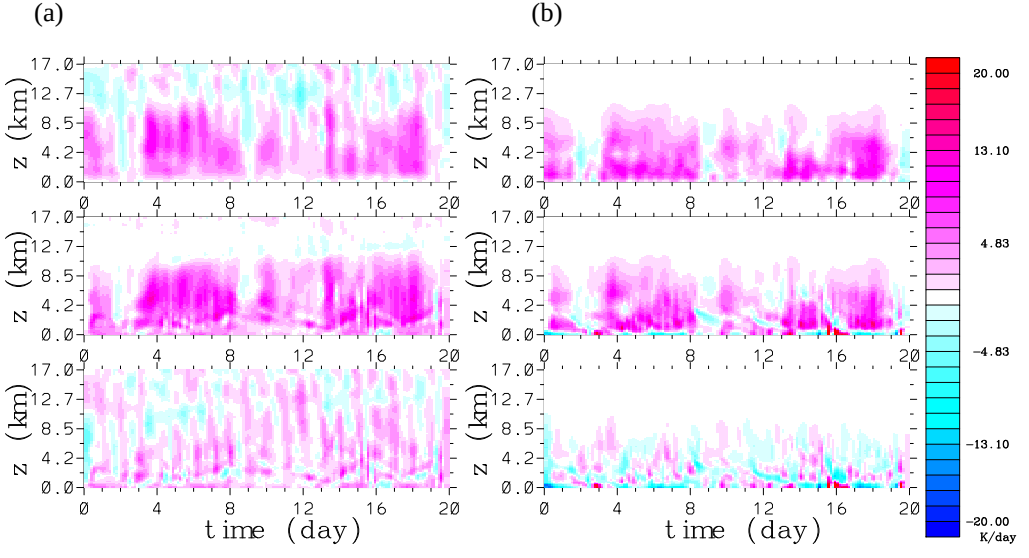

Fig. 13. Time-height section for **(a)** apparent heat source, Q_1 and apparent moisture sink, Q_2 during the GATE Phase III. From top to bottom: observation, the NAM-SCA stand-alone case with $\Delta x = 16\,\mathrm{km}$, $L = 32\,\mathrm{km}$, and the difference of the two.

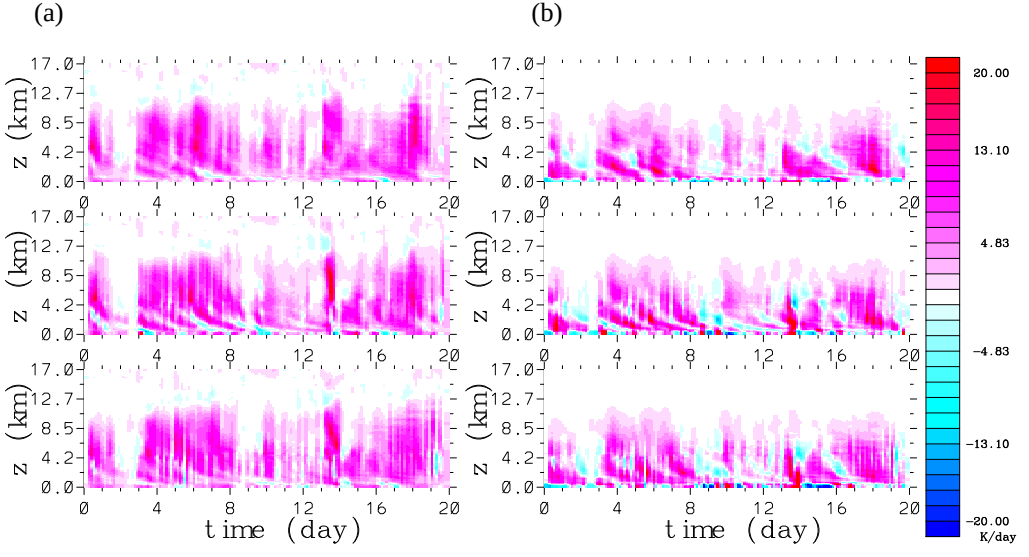

Fig. 14. Further examples of time-height sections for **(a)** apparent heat source, Q_1 and **(b)** apparent moisture sink, Q_2 during the GATE Phase III from NAM-SCA stand-alone simulations. The cases are from top to bottom: $\Delta x = 0.5\,\mathrm{km}$, $L = 512\,\mathrm{km}$ (top), $\Delta x = 1\,\mathrm{km}$, $L = 256\,\mathrm{km}$ (middle), $\Delta x = 4\,\mathrm{km}$, $L = 256\,\mathrm{km}$ (bottom).

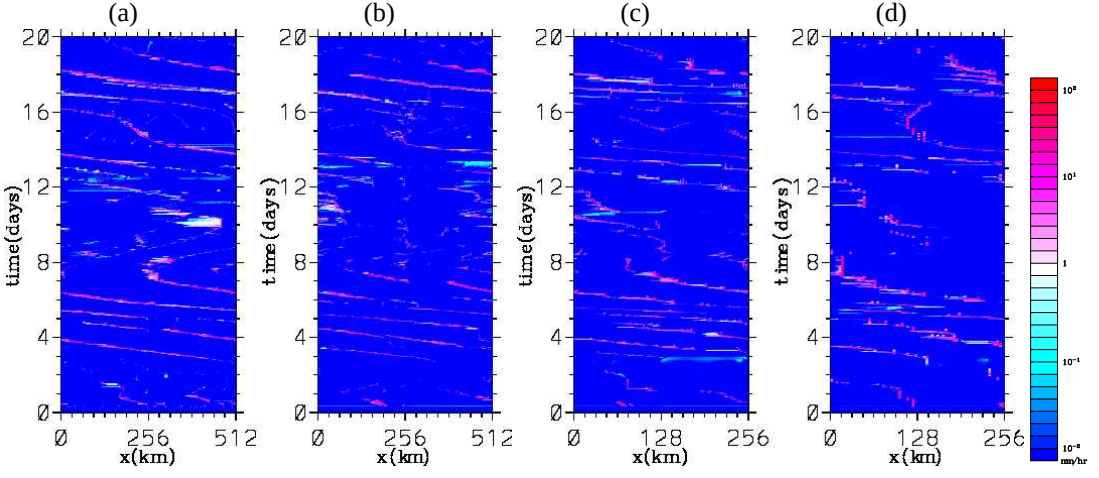

Fig. 15. The precipitation rate plotted as a function of the longitude and time for the GATE case with: **(a)** $\Delta x = 0.5\,\mathrm{km}$ and $L = 512\,\mathrm{km}$, **(b)** $\Delta x = 1\,\mathrm{km}$ and $L = 512\,\mathrm{km}$, **(c)** $\Delta x = 2\,\mathrm{km}$ and $L = 256\,\mathrm{km}$. and **(d)** $\Delta x = 4\,\mathrm{km}$ and $L = 256\,\mathrm{km}$.

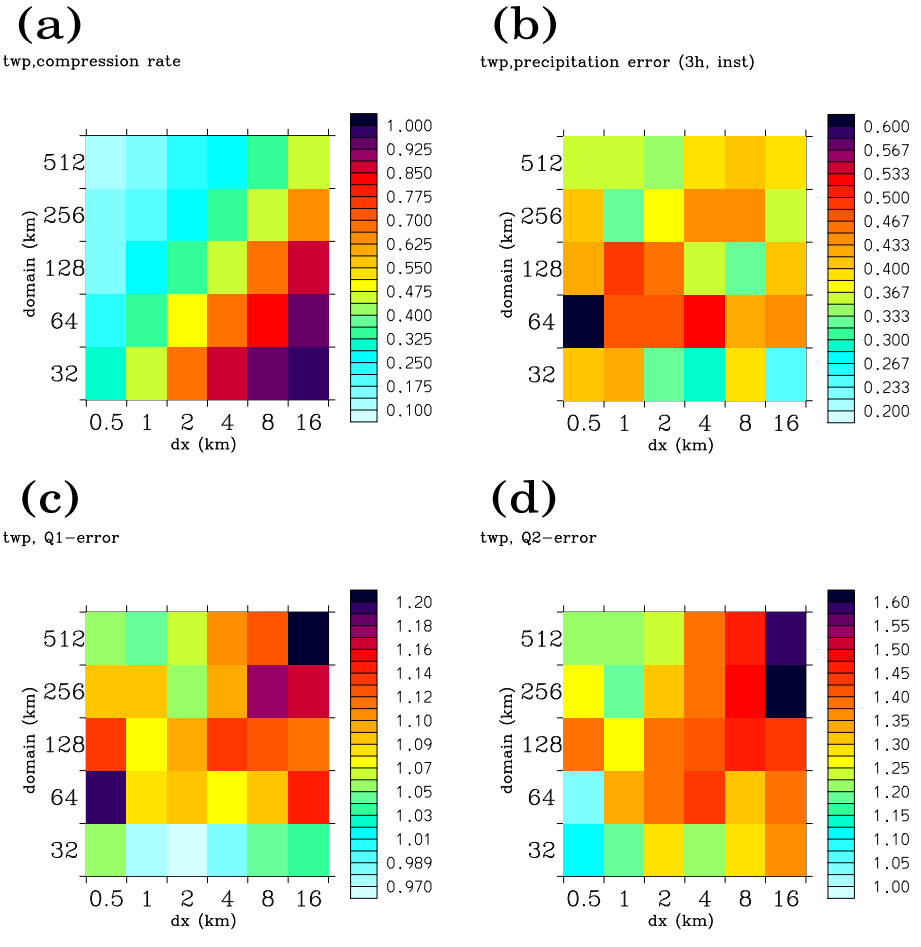

Fig. 16. Summary of stand-alone TWP-ICE case. The same format as in Fig. 11.

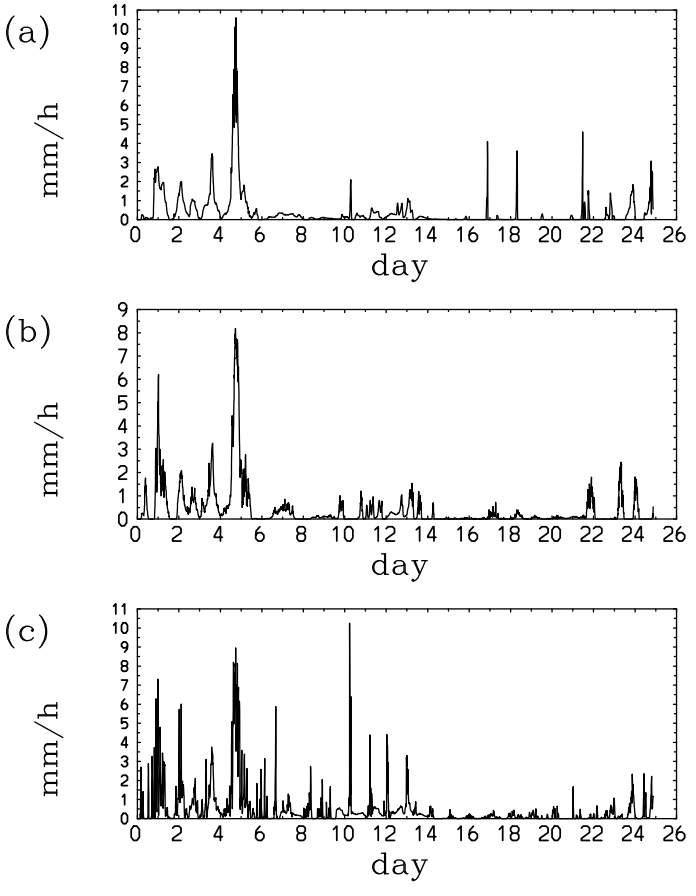

Fig. 17. The simulated domain-mean precipitation time series for the stand-alone TWP-ICE case: **(a)** $\Delta x = 16\,\mathrm{km}$, $L = 32\,\mathrm{km}$ (best simulated precipitation), **(b)** $\Delta x = 0.5\,\mathrm{km}$, $L = 512\,\mathrm{km}$ (highest-resolution with largest domain), **(c)** $\Delta x = 0.5\,\mathrm{km}$, $L = 64\,\mathrm{km}$ (worst simulated precipitation).

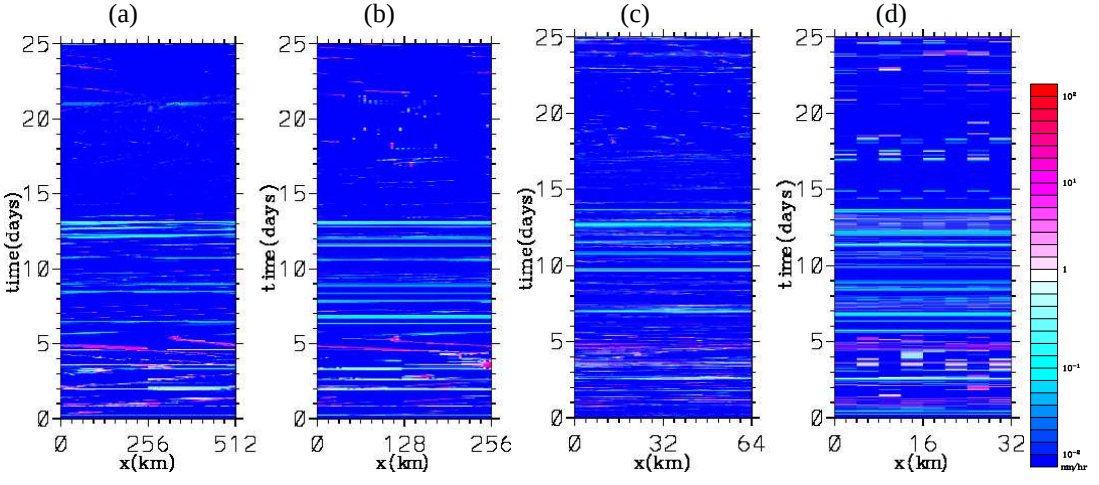

Fig. 18. The precipitation rate plotted as a function of the longitude and time for the cases for the stand–alone TWP–ICE cases: **(a)** $\Delta x = 0.5\,\mathrm{km}$, $L = 512\,\mathrm{km}$, **(b)** $\Delta x = 4\,\mathrm{km}$, $L = 256\,\mathrm{km}$, **(c)** $\Delta x = 0.5\,\mathrm{km}$, $L = 64\,\mathrm{km}$, and **(d)** $\Delta x = 2\,\mathrm{km}$, $L = 32\,\mathrm{km}$. The precipitation rates are shown in logarithmic scale for the range of $10^{-2}\,\mathrm{mm\,h^{-1}}$ to $10^{2}\,\mathrm{mm\,h^{-1}}$ with the color ranging from blue (lowest) to red (highest) with a middle value shown in white.

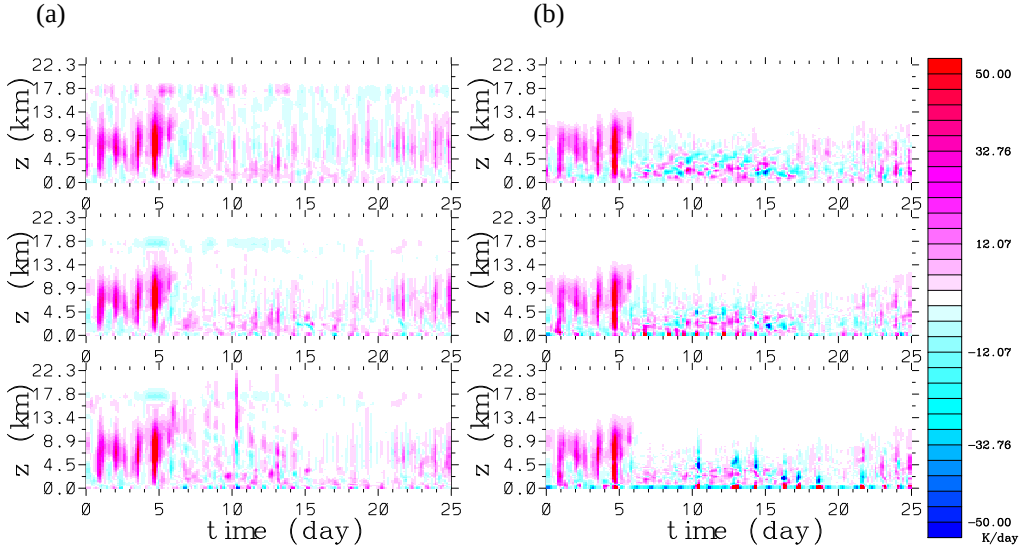

Fig. 19. The time-height section of the TWP-ICE case for the observation (top), the best simulation (middle), and one of the worst simulations (bottom) in term of the errors for (**a**: left) apparent heat source, Q_1, and for (**b**: right) apparent moisture sink, Q_2, respectively. The cases shown are: (**a**: middle) $\Delta x = 2\,\mathrm{km}$, $L = 32\,\mathrm{km}$, (**a**: bottom) $\Delta x = 0.5\,\mathrm{km}$, $L = 64\,\mathrm{km}$, (**b**: middle) $\Delta x = 0.5\,\mathrm{km}$, $L = 64\,\mathrm{km}$, (**b**: bottom) $\Delta x = 16\,\mathrm{km}$, $L = 256\,\mathrm{km}$.

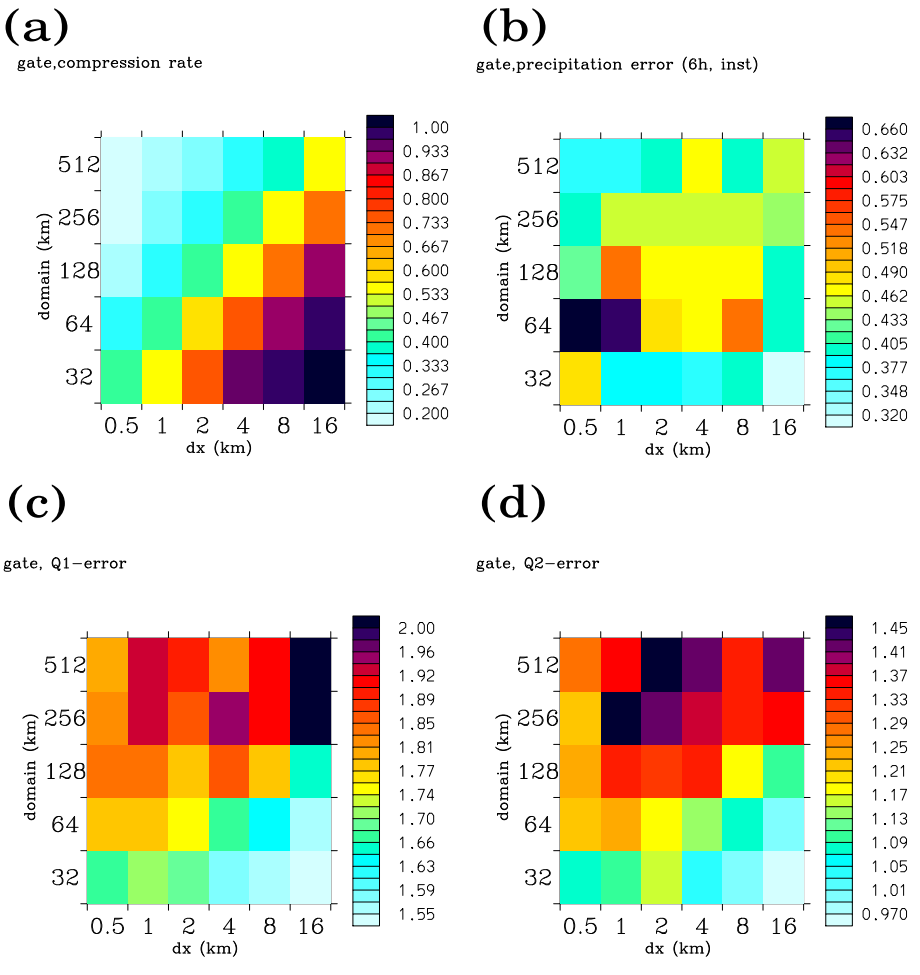

Fig. 20. Summary of the ECHAM GATE case. The errors are shown under a normalization by those with the default physics results. Otherwise, the same format as in Fig. 11.

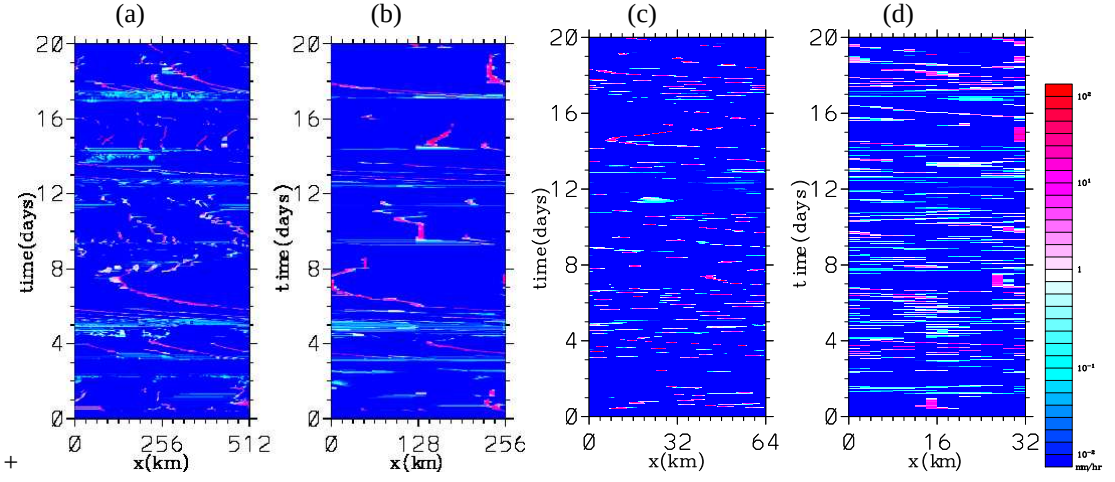

Fig. 21. The same as Fig. 15 but for NAM-SCA with ECHAM SCM for the GATE case: the precipitation rate from ECHAM GATE simulations with NAM-SCA plotted as a function of the longitude and time with: **(a)** $\Delta x = 0.5\,\mathrm{km}$ and $L = 512\,\mathrm{km}$, **(b)** $\Delta x = 4\,\mathrm{km}$ and $L = 256\,\mathrm{km}$, **(c)** $\Delta x = 0.5\,\mathrm{km}$ and $L = 64\,\mathrm{km}$. and **(d)** $\Delta x = 2\,\mathrm{km}$ and $L = 32\,\mathrm{km}$. The precipitation rates are shown in logarithmic scale for the range of $10^{-2}\,\mathrm{mm\,h^{-1}}$ to $10^{2}\,\mathrm{mm\,h^{-1}}$ with the color ranging from blue (lowest) to red (highest) with a middle value shown in white.

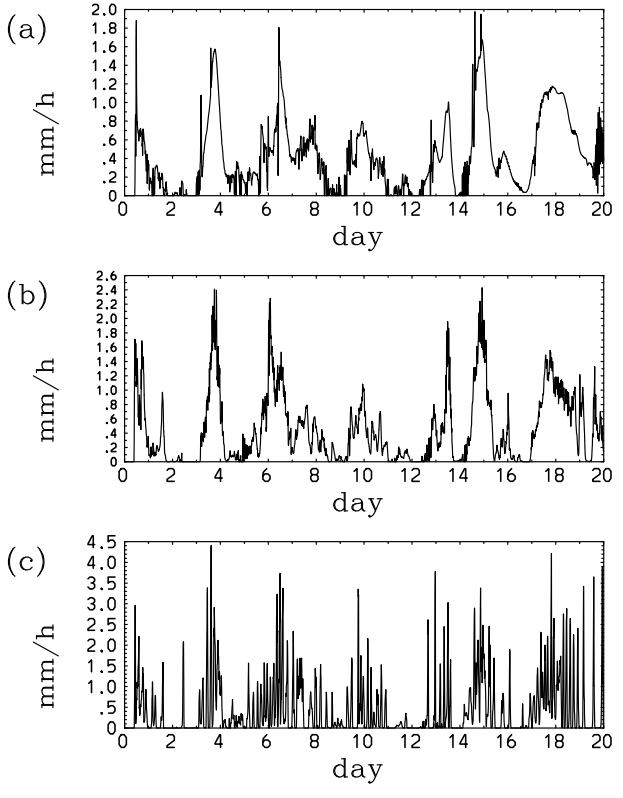

Fig. 22. The same as Fig. 12 bur for the for the GATE case obtained by ECHAM simulations with NAM-SCA: the domain-mean precipitation time series for the GATE case obtained by ECHAM simulations with NAM-SCA: **(a)** $\Delta x = 16\,\mathrm{km}$, $L = 32\,\mathrm{km}$ (best simulated precipitation), **(b)** $\Delta x = 0.5\,\mathrm{km}$, $L = 512\,\mathrm{km}$ (highest-resolution with largest domain), **(c)** $\Delta x = 0.5\,\mathrm{km}$, $L = 64\,\mathrm{km}$ (worst simulated precipitation).

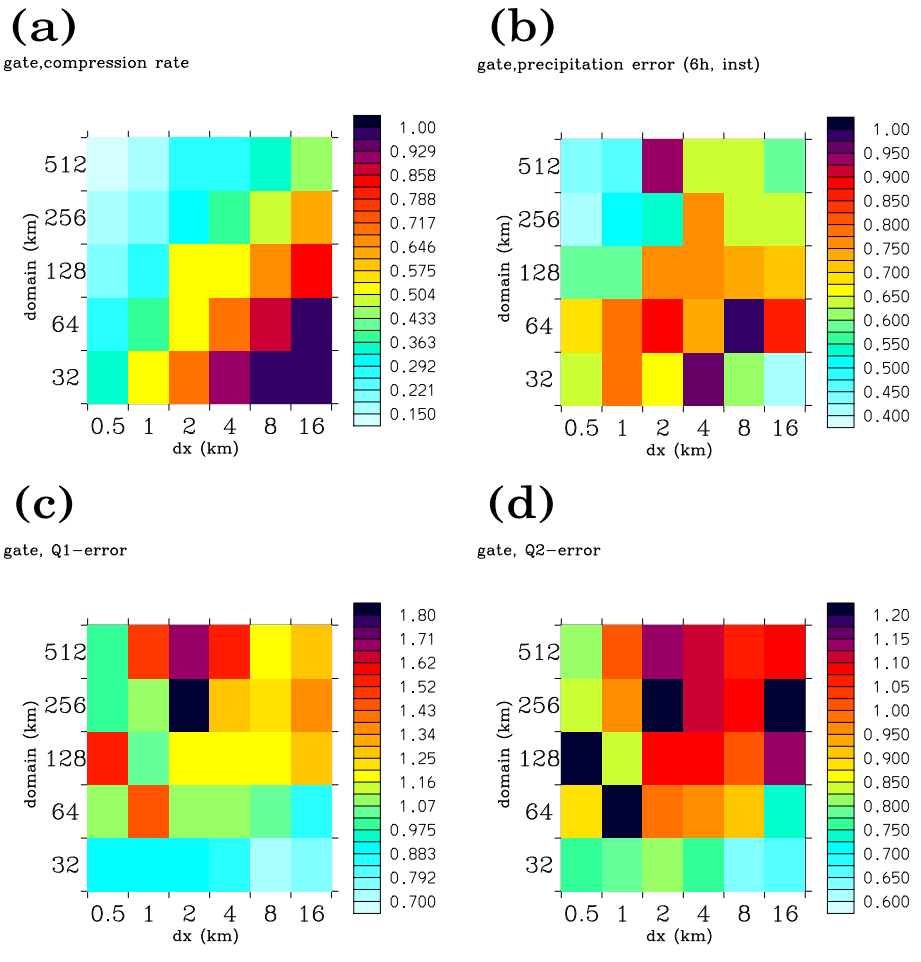

Fig. 23. Summary of the ACCESS GATE case. The errors are shown under a normalization by those with the default physics results. Otherwise, the same format as in Fig. 11.

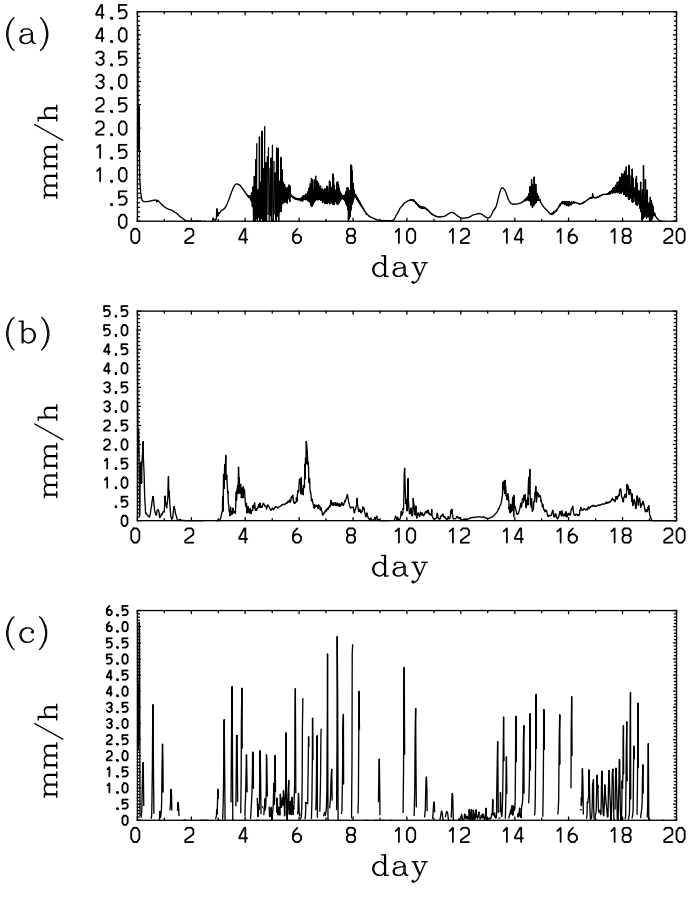

Fig. 24. The same as Fig. 12 bur for for the GATE case obtained by ACCESS simulations with NAM-SCA. From top to bottom: **(a)** $\Delta x = 16\,\mathrm{km}$, $L = 32\,\mathrm{km}$ (best simulated precipitation); **(b)** $\Delta x = 0.5\,\mathrm{km}$, $L = 512\,\mathrm{km}$; **(c)** $\Delta x = 8\,\mathrm{km}$, $L = 64\,\mathrm{km}$ (the worst case).

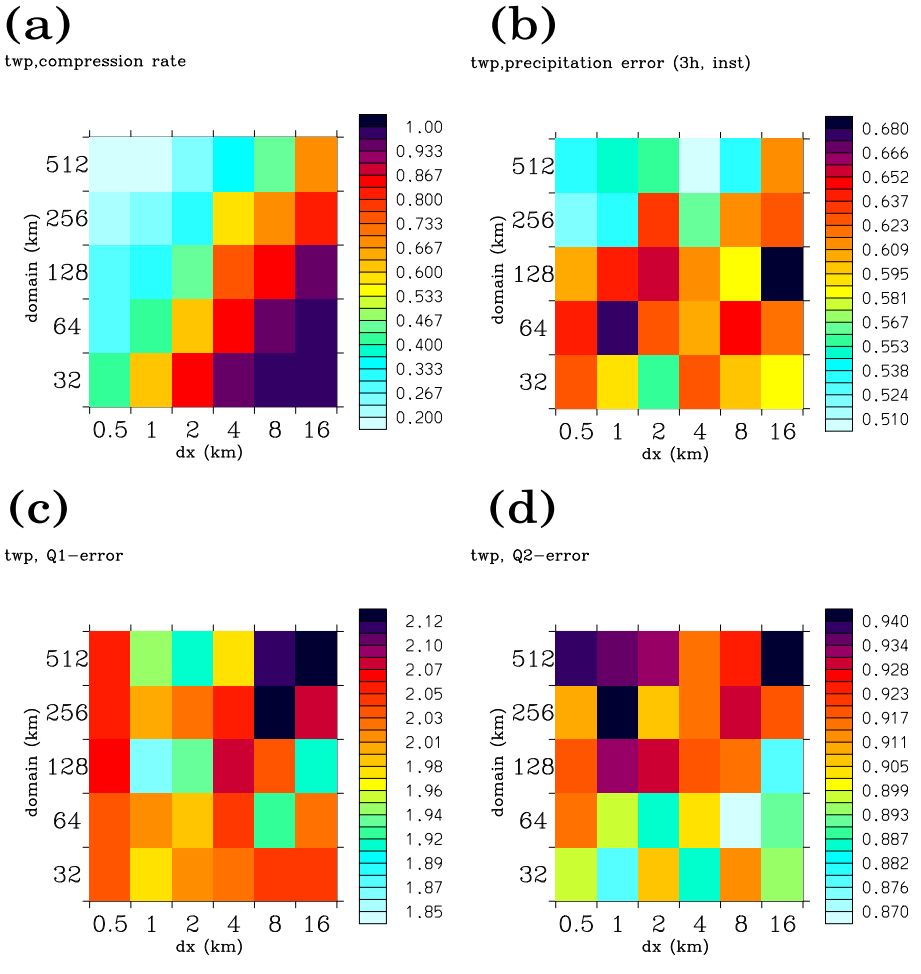

Fig. 25. Summary of the ECHAM TWP-ICE case. The same format as in Fig. 20.

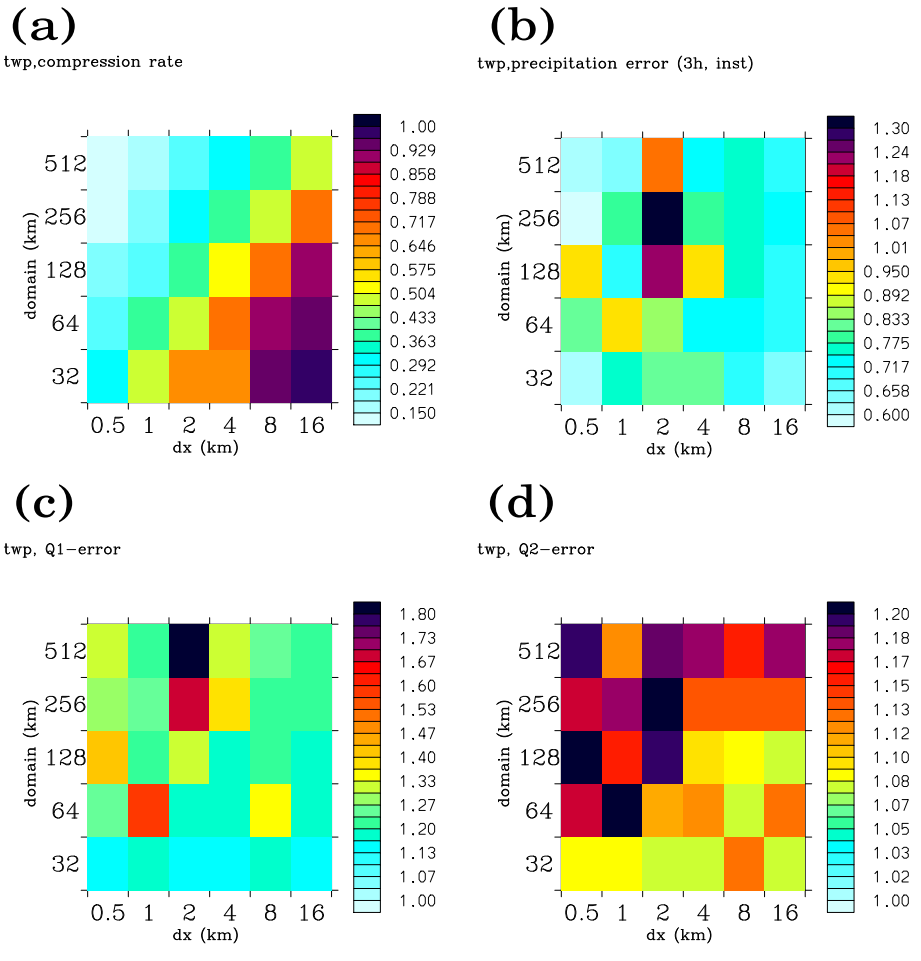

Fig. 26. Summary of the ACCESS TWP-ICE case. The same format as in Fig. 23.

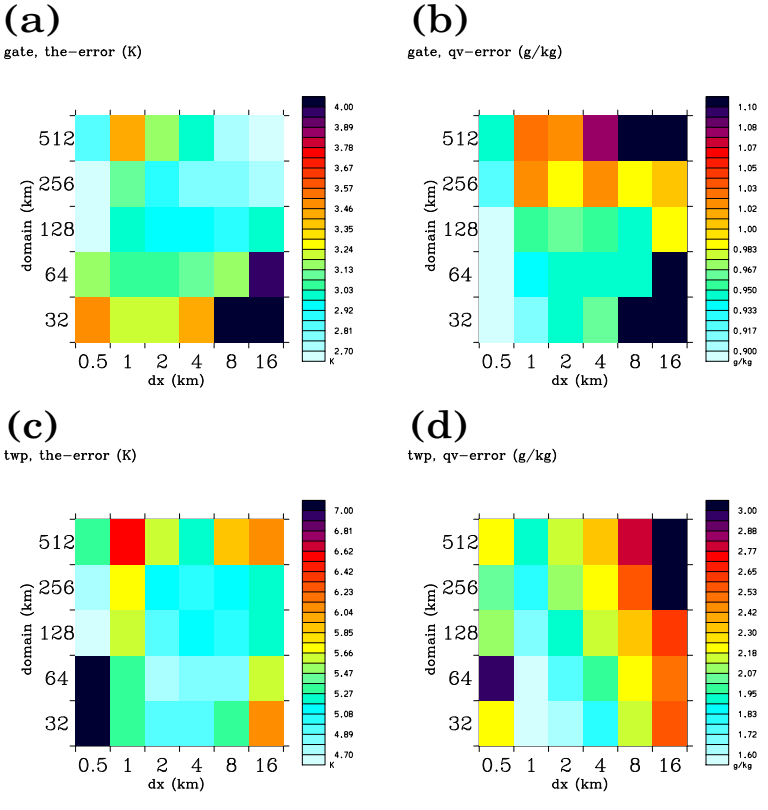

Fig. 27. Summary of the prediction errors in stand-alone **(a, b)** GATE and **(c, d)** TWP-ICE cases. RMS prediction errors for the potential temperature (K: **a**, **c**) and the moisture mixing ration ($\mathrm{g kg}^{-1}$: **b**, **d**) are shown as functions of the resolution, Δx (horizontal axis) and the domain size, L (vertical axis).

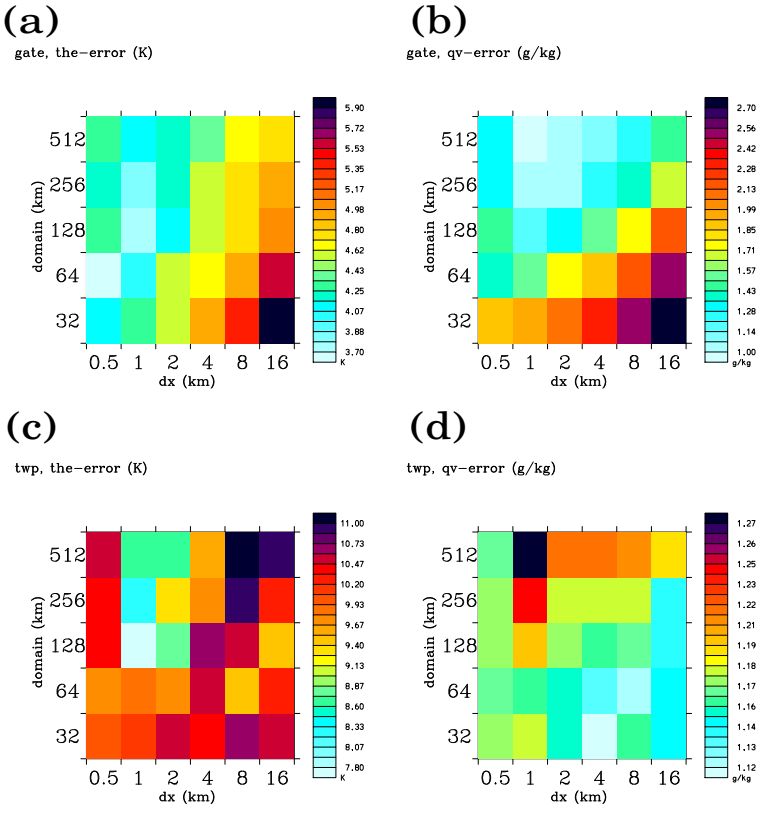

Fig. 28. Summary of the prediction errors under implementation into ECHAM for **(a, b)** GATE and **(c, d)** TWP-ICE cases. RMS prediction errors for the potential temperature (K: **a**, **c**) and the moisture mixing ration ($\mathrm{g\,kg^{-1}}$: **b**, **d**) are shown as functions of the resolution, Δx (horizontal axis) and the domain size, L (vertical axis).